

Cortical regulation of two-stage rapid eye movement sleep

Received: 9 February 2022

Yufan Dong  ^{1,2}, Jiaqi Li¹, Min Zhou  ^{1,2}, Yihui Du¹ & Danqian Liu  ^{1,3} 

Accepted: 5 October 2022

Published online: 17 November 2022

 Check for updates

Rapid eye movement (REM) sleep is a sleep state characterized by skeletal muscle paralysis and cerebral cortical activation. Yet, global cortical dynamics and their role in regulating REM sleep remain unclear. Here we show that in mice, REM sleep is accompanied by highly patterned cortical activity waves, with the retrosplenial cortex (RSC) as a major initiation site. Two-photon imaging of layer 2/3 pyramidal neurons of the RSC revealed two distinct patterns of population activities during REM sleep. These activities encoded two sequential REM sleep substages, characterized by contrasting facial movement and autonomic activity and by distinguishable electroencephalogram theta oscillations. Closed-loop optogenetic inactivation of RSC during REM sleep altered cortical activity dynamics and shortened REM sleep duration via inhibition of the REM substage transition. These results highlight an important role for the RSC in dictating cortical dynamics and regulating REM sleep progression.

The sleep–wake cycle, including rapid eye movement (REM) sleep and non-rapid eye movement (NREM) sleep, is generally considered to be primarily regulated by distributed subcortical circuits^{1–4}, whereas cortical regions are involved in generating sleep-related electroencephalogram (EEG) oscillations^{5–8}. However, recent studies showed that cortical neurons could be actively involved in NREM sleep generation and homeostatic sleep regulation^{9,10}. Although cortical activation during REM sleep is considered to be associated with vivid dreaming^{11–13}, the role for the cortex in REM sleep regulation remains unknown. Here we show that the retrosplenial cortex (RSC) is selectively activated and initiates cortex-wide calcium waves during REM sleep. Two-photon imaging of cortical neurons showed that the layer 2/3 (L2/3) but not L5 pyramidal neurons were activated during REM sleep. Furthermore, RSC L2/3 neuronal activation during REM sleep exhibited two non-overlapping temporal profiles, carried by two dynamic neuronal populations. The transition of activity patterns temporally matched the transition of two sequential REM substages, identified by contrasting facial movement and distinguishable EEG theta oscillation. Closed-loop optogenetic inactivation of excitatory neurons in RSC during REM sleep shortened REM sleep duration, via inhibition of the REM substage transition. By contrast, inactivation of other cortical areas—the secondary motor cortex (M2) or the anterior cingulate cortex (ACC)—had

no effect on REM sleep duration. These results uncover two distinct substages in REM sleep and highlight a role for RSC in regulating REM substage transition.

Results

The RSC is selectively activated during REM sleep

To examine whether and how the cortex participates in REM sleep regulation, we first monitored global neuronal activity across the sleep–wake cycle in head-fixed mice through cortex-wide Ca^{2+} imaging^{14,15} (Fig. 1a). We implanted a chronic transparent window covering the entire dorsal cortex of the *Thy1-GCaMP6s* mice¹⁶ and recorded Ca^{2+} signals together with EEG, electromyogram (EMG) and video recording (Fig. 1a). After extensive habituation, head-fixed mice exhibited similar REM sleep as mice in freely moving conditions, but they took longer to fall asleep and showed fragmented NREM sleep^{17,18} (Supplementary Fig. 1). We found that cortical activity during REM sleep was higher than that during other sleep states, with posterior and medial cortical regions more active (Fig. 1b). Spatial independent component analysis^{15,19} (sICA) identified 11 main functional cortical modules (Fig. 1c) that corresponded to anatomically defined brain areas, including the superficial layer of the RSC (RSCs), primary visual cortex (V1), ACC and frontal association area (FrA). During REM sleep, the activity of the

¹Institute of Neuroscience, Center for Excellence in Brain Science and Intelligence Technology, Chinese Academy of Sciences, Shanghai, China.

²University of Chinese Academy of Sciences, Beijing, China. ³Shanghai Center for Brain Science and Brain-Inspired Intelligence Technology, Shanghai, China.  e-mail: dqliu@ion.ac.cn

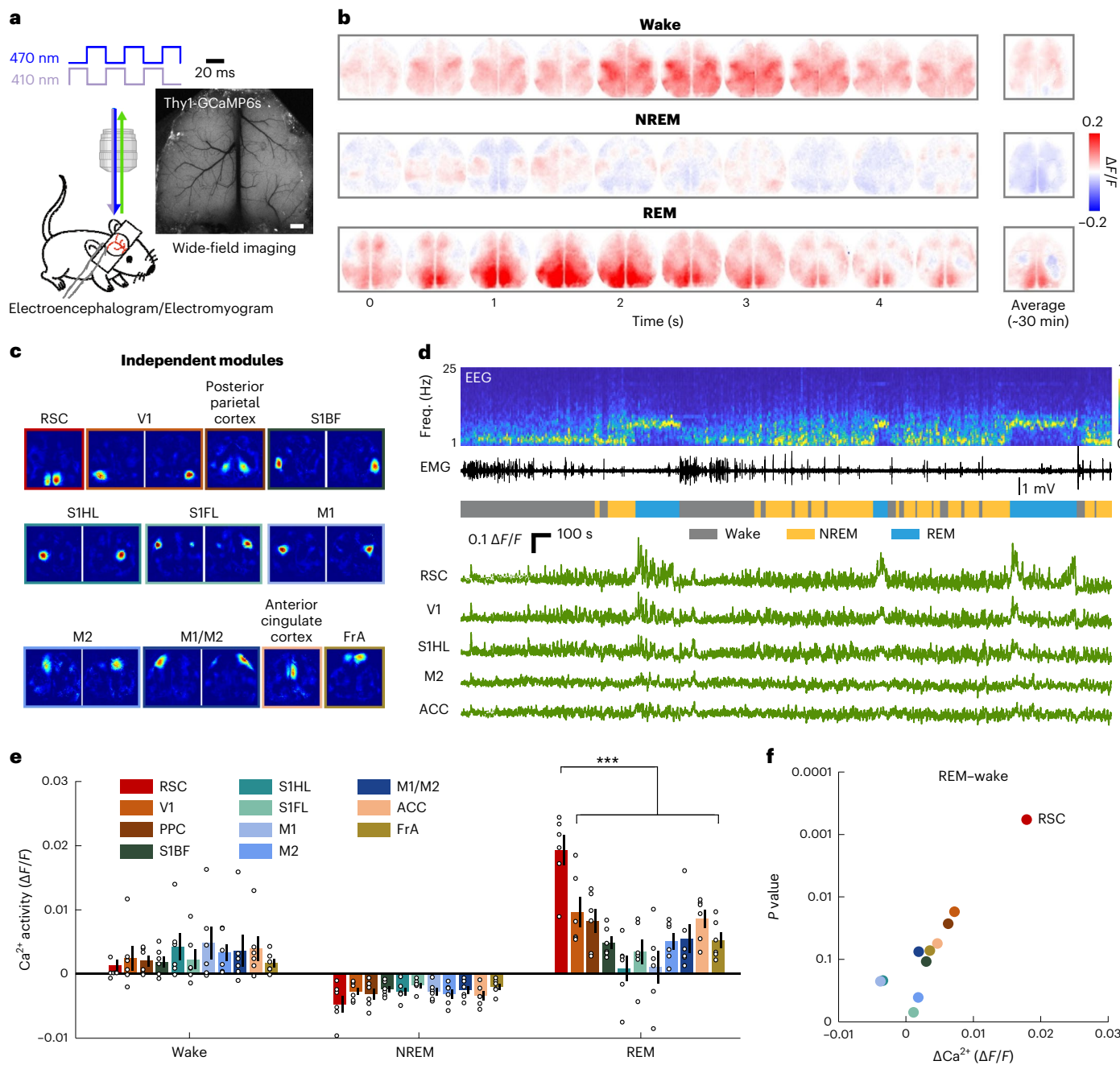


Fig. 1 | Selective activation of the retrosplenial cortex (RSC) during REM sleep revealed by cortex-wide Ca^{2+} imaging. a, Schematic for wide-field Ca^{2+} imaging in head-fixed mice and fluorescence image from a *Thy1*-GCaMP6s mouse. Scale bar, 1 mm. **b**, Example of cortex-wide activity across sleep–wake states. Shown are images sequences of 410-nm-corrected $\Delta F/F \text{Ca}^{2+}$ signals over 5 s and average fluorescence from a 30-min recording session, in wake, non-rapid eye movement (NREM) and rapid eye movement (REM) sleep. **c**, Eleven modules obtained by sICA (Methods). Bilateral symmetric modules are grouped into

RSC was distinctly higher than that of other cortical areas ($P < 0.005$ for comparisons of RSC with ten other areas; Fig. 1d,e and Extended Data Fig. 1a,b). Moreover, although most areas were more active in REM sleep than in the wake state, the difference was much higher in the RSC ($P < 0.001$; Fig. 1f, Extended Data Fig. 1c–e and Supplementary Fig. 2). We further performed fiber photometry recording to monitor Ca^{2+} activity simultaneously at four cortical regions, including the superficial layer of RSC (RSCs), granular layer of the RSC (RSCg), the

one module. SIBF, somatosensory barrel field; SIFL, somatosensory forelimb; SIHL, somatosensory hindlimb. **d**, Example calcium traces of five cortical areas together with EEG spectrogram, EMG trace and brain states. **e**, Average calcium activity during wake state, NREM and REM sleep ($n = 6$ sessions from 5 mice). Error bars denote the s.e.m.; $***P < 0.001$, one-way analysis of variance (ANOVA) with Tukey's multiple-comparison correction. **f**, Activity difference between REM sleep and wake state, with statistical significance (two-sided paired t -test) plotted against the difference in average $\text{Ca}^{2+} \Delta F/F$ values.

granular layer of ACC (ACCg) and the insula cortex, in freely moving *Thy1-GCaMP6s* mice (Supplementary Fig. 3a–c). We found that the RSC also showed the highest Ca^{2+} activity during REM sleep under freely moving conditions (Supplementary Fig. 3d,e). Taken together, these results indicate that the RSC was selectively activated during REM sleep.

We next performed Granger causality analysis to quantify the activation sequence of cortical areas²⁰. This analysis showed that during REM sleep, but not during the wake state, RSC activity preceded

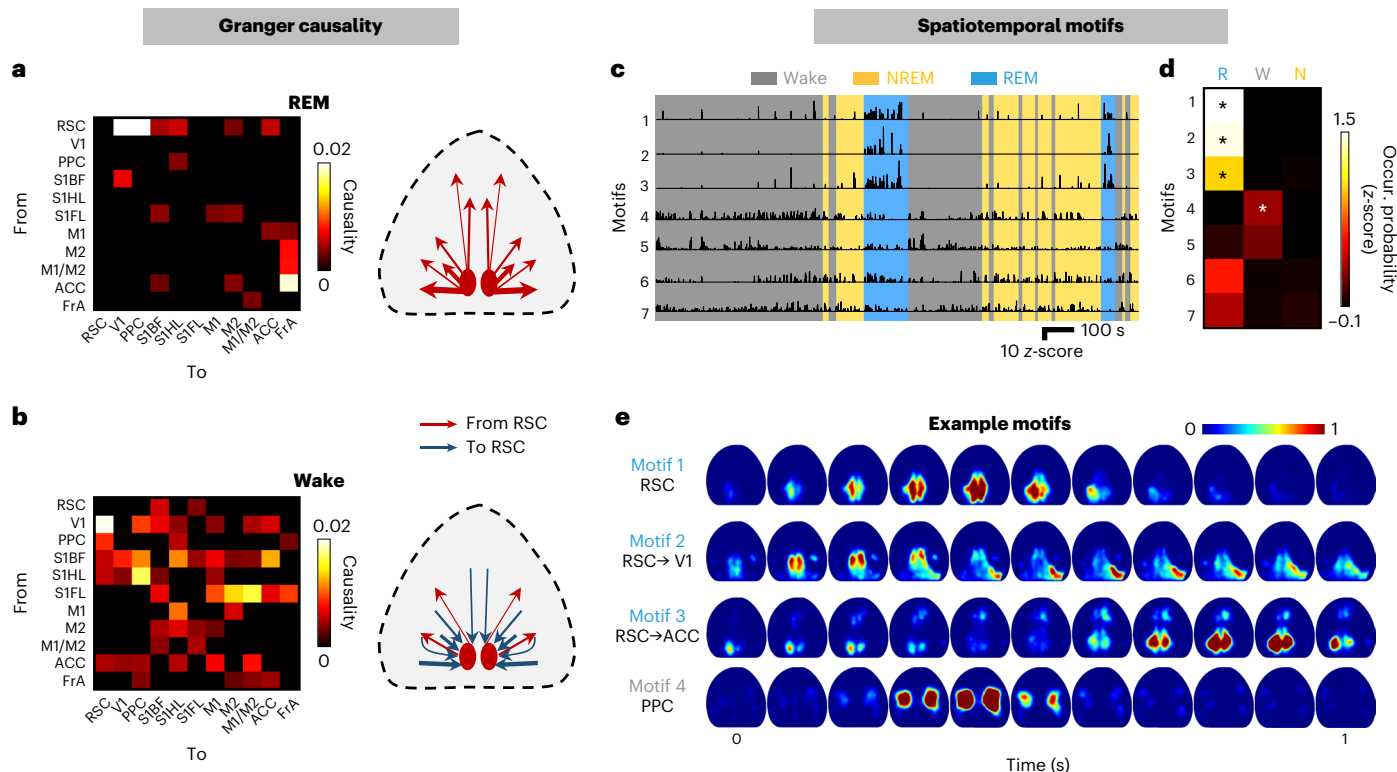


Fig. 2 | RSC is a major initiation site for cortical Ca^{2+} waves during REM sleep.

a, Matrix of Granger causality between each pair of 11 cortical areas during REM sleep ($n = 12$ REM episodes from 5 mice). Note that the uppermost row is the causality from the RSC to the other 10 areas. Causality with $P < 0.01$ (Granger F test) was shown after correction for multiple comparisons by false discovery rate. Summary of causality between the RSC and other cortical modules. Red arrows indicate from the RSC to other modules; blue arrows indicate from other modules to the RSC. **b**, Similar to **a**, but for Granger causality during the wake state. **c**, Occurrence probability of seven common spatiotemporal activity

motifs identified by seqNMF, across sleep and wake states. Motif intensity was measured by temporal weightings of each motif. **d**, Color map showing the occurrence probability of seven motifs, averaged across $n = 6$ recording sessions from 5 mice. R, REM; W, wake; N, NREM. An asterisk denotes a significantly higher probability in each state than in other states at $P < 0.05$, two-sided paired t -test. **e**, Time courses of example motifs 1–4 in **c** and **d** showing spatiotemporal patterns of neuronal Ca^{2+} activity across the dorsal cortex. The intensity scale was normalized for each motif separately. Cortical activity in REM-active motifs 1–3 all initiated at the RSC.

the activity of many other cortical areas (Fig. 2a,b and Extended Data Fig. 2a–d), suggesting an initiating role of the RSC in cortical dynamics during REM sleep. To further explore the spatiotemporal dynamics of cortical activity, seqNMF—an unsupervised algorithm for temporal sequence discovery—was used to uncover repeated spatiotemporal patterns ('motifs') of cortical Ca^{2+} fluctuations and waves^{21,22} (Methods). Seven motifs were commonly identified across recording sessions and animals (Fig. 2c) that showed higher occurrence probability during either REM sleep or wake state (Fig. 2d). Interestingly, activity in all REM-active motifs initiated at the RSC, followed by local sustained activity, lateral propagation to V1 or anterior propagation to ACC (see example motifs in Fig. 2e). By contrast, motifs that were active in the wake state originated from diverse cortical regions, such as the parietal cortex (Fig. 2e and Extended Data Fig. 2e). Thus, REM sleep was associated with unique patterns of cortical waves, and the RSC seems to play a role in initiating cortical waves during REM sleep.

Two distinct patterns of RSC L2/3 neuronal activation during REM sleep

We next performed two-photon Ca^{2+} imaging to examine RSC activation at the single-neuron level during REM sleep. L2/3 pyramidal neurons in the RSCs or M2 of *Thy1-GCaMP6s* mice, or RSC L5 neurons labeled with GCaMP6s in the *Rbp4*^{Cre} mice were imaged throughout the sleep–wake cycle (Fig. 3a,b and Extended Data Fig. 3a–f). We found that RSC L2/3 neurons were more active during REM sleep than other states (Fig. 3b,c). The percentage of REM-active neurons in L2/3 was much

higher in the RSC than in M2 (63.4% versus 28.3%, $P < 0.001$; Extended Data Fig. 3g–i). By contrast, the majority of RSC L5 neurons were inactive during REM sleep (72.3%; Extended Data Fig. 3a–c,g–i). Thus, the RSC exhibited layer-specific activation during REM sleep, consistent with a recent study that showed dense cFos labeling specifically in the RSCs after REM sleep hypersomnia²³. Furthermore, on average, the activity of REM-active RSC L2/3 neurons gradually increased after REM sleep onset and declined before entering the wake state (Extended Data Fig. 3j), suggesting that these neurons may contribute to the maintenance of REM sleep.

In the above study, we noted divergent temporal patterns of RSC L2/3 neuronal activation during REM sleep (Fig. 3b). Measurements of the pairwise correlation coefficient (CC) of neuronal activity during each REM episode, followed by unsupervised k -means clustering of CCs, indeed revealed two distinct populations of RSC neurons (Fig. 3d and Extended Data Fig. 4a–c). These two populations exhibited a largely nonoverlapping temporal profile: type I neurons were active within the first -30 s of REM sleep, whereas type II neurons were activated at the later stage of REM sleep (Fig. 3e and Extended Data Fig. 4d). Notably, the identity of individual neurons in these two populations varied across REM episodes (Extended Data Fig. 4e).

Analysis of mouse facial movements reveals two distinct substages of REM sleep

By inspecting mouse facial characteristics during REM sleep (Extended Data Fig. 1c), we found that the eye, whisker and cheek movements also

exhibited two distinguishable patterns (Fig. 3f). Following a previous method for mouse facial expression analysis²⁴, we obtained the histogram of oriented gradients (HOGs; Methods) of video frames, followed by hierarchical clustering of the pairwise CCs of HOGs between frames (Fig. 3g). The results revealed two main clusters during REM sleep, corresponding to a state with and a state without active facial movements, defined here as active REM (aREM) and quiescent REM (qREM) sleep, respectively (Fig. 3f,g, Extended Data Fig. 5 and Supplementary Video 1). The two substates were associated with distinct EEG theta oscillations: power in the low theta band (6.5–7.5 Hz) was higher during qREM, whereas power in the high theta band 8.2–10 Hz was higher during aREM (Extended Data Fig. 5a–c). Moreover, we found that heart rate variability, respiration rate and hemodynamics—reflecting activity of the autonomic nervous system—were all significantly different between these two substates (Extended Data Fig. 5f–h), such that sympathetic tone was higher (including lower heart rate variability) during aREM than during qREM.

To investigate whether similar REM sleep substates also exist in natural REM sleep, we performed EMG recording from the masseter muscle, together with the neck muscle EMG and EEG in freely moving mice (Extended Data Fig. 6a,b). We found that there was a significantly higher EMG power of the masseter muscle in the later stage of REM sleep, corresponding to the aREM substate (Extended Data Fig. 6b–d). Moreover, the qREM and aREM substates identified in freely moving mice also exhibited distinct EEG theta oscillations and different heart rate variability (Extended Data Fig. 6c–g), similarly to our observations in head-fixed mice. The qREM and aREM could be related, although are not identical, to tonic and phasic REM phases in human studies^{25,26}, where phasic REM is defined as transient periods of eye movements, and tonic REM represents the period without eye movement. However, aREM here represents a sustained ‘activated’ substate with not only eye movements but also whisker and facial movements, and qREM represents a state without any apparent movement. A REM sleep episode began with a short period of qREM (usually <30 s) and progressed through aREM before the wake state (Fig. 3f,g, Extended Data Figs. 5 and 6 and Supplementary Video 1). Thus, similarly to NREM sleep having various substages²⁷, REM sleep is also composed of two distinct substages.

RSC L2/3 neuronal population activity encodes two REM sleep substages

Importantly, the qREM-to-aREM transition temporally matched the transition of RSC neuronal population activity patterns (Fig. 3h and Extended Data Fig. 4d–f). The type I and II populations were active in qREM and aREM, respectively, and showed negative and positive CCs, respectively, with the aREM substage (Fig. 3i). As a previous functional magnetic resonance imaging study revealed eye movement-locked activation in the RSC during sleep in humans²⁸, we also measured the CCs of each population with eye movements. However, the CCs of both populations with eye movements were close to zero ($P > 0.7$; Extended Data Fig. 4g), indicating that their activation during aREM was not time-locked to phasic eye movements. To further examine whether the RSC population activity encodes REM sleep substages,

we trained a support vector machine (SVM) classifier to decode qREM and aREM using neuronal activity of randomly selected sets of RSC neurons ($n = 1$ to 100). The decoding accuracy improved with increasing n and exceeded 90% when n was larger than 60 (Fig. 3j). By contrast, the prediction accuracy of RSC neuronal activity for eye movements was much lower ($P < 0.0001$; Fig. 3j). These results demonstrated that the RSC population activity carries enriched information encoding the two substages of REM sleep.

RSC inactivation alters cortical activity dynamics during REM sleep

To examine whether the RSC plays an active role in REM sleep, we performed optogenetic inactivation experiments. We first characterized the effect of RSC inactivation on cortical dynamics. Adeno-associated virus expressing halorhodopsin (NpHR) fused with mCherry (AAV-CaMKIIα-NpHR3.0-mCherry) was injected bilaterally into the L2/3 of the RSC in *Thy1-GCaMP6s* mice (Fig. 4a and Extended Data Fig. 7a), allowing simultaneous GCaMP6s imaging (with blue light) and RSC inhibition (with yellow light). In the above experiment (Supplementary Video 1), we observed that the mouse pupil size started to decrease before REM sleep onset and remained at its smallest size during the entire REM sleep period¹⁸ (Supplementary Fig. 4a). We therefore used real-time characterization of the pupil size to predict REM sleep, such that we could initiate light at ~30 s before the onset of REM sleep and maintain it throughout the REM episode (Supplementary Fig. 4b–d). We found that RSC activity was markedly reduced by the optogenetic inactivation during REM sleep (‘RSC_{REM} inactivation’, Fig. 4b,c and Extended Data Fig. 7b,c). By analyzing cortex-wide Ca^{2+} activities, we found that the seven common activity motifs described above (Fig. 2c–e and Extended Data Fig. 2e) were still present during RSC_{REM} inactivation (Fig. 4d). However, the intensity of the three RSC-initiated motifs was significantly reduced ($P < 0.05$; Fig. 4e), whereas that of the posterior parietal cortex (PPC) motif was slightly elevated. Moreover, under RSC_{REM} inactivation, we observed two new motifs with Ca^{2+} activity initiated at FrA, followed by either sustained local FrA activation or propagated waves to posterior cortical regions (Extended Data Fig. 7d–f). These data showed that RSC inactivation markedly reorganized global cortical activity dynamics during REM sleep.

The RSC is required for substage transition during REM sleep

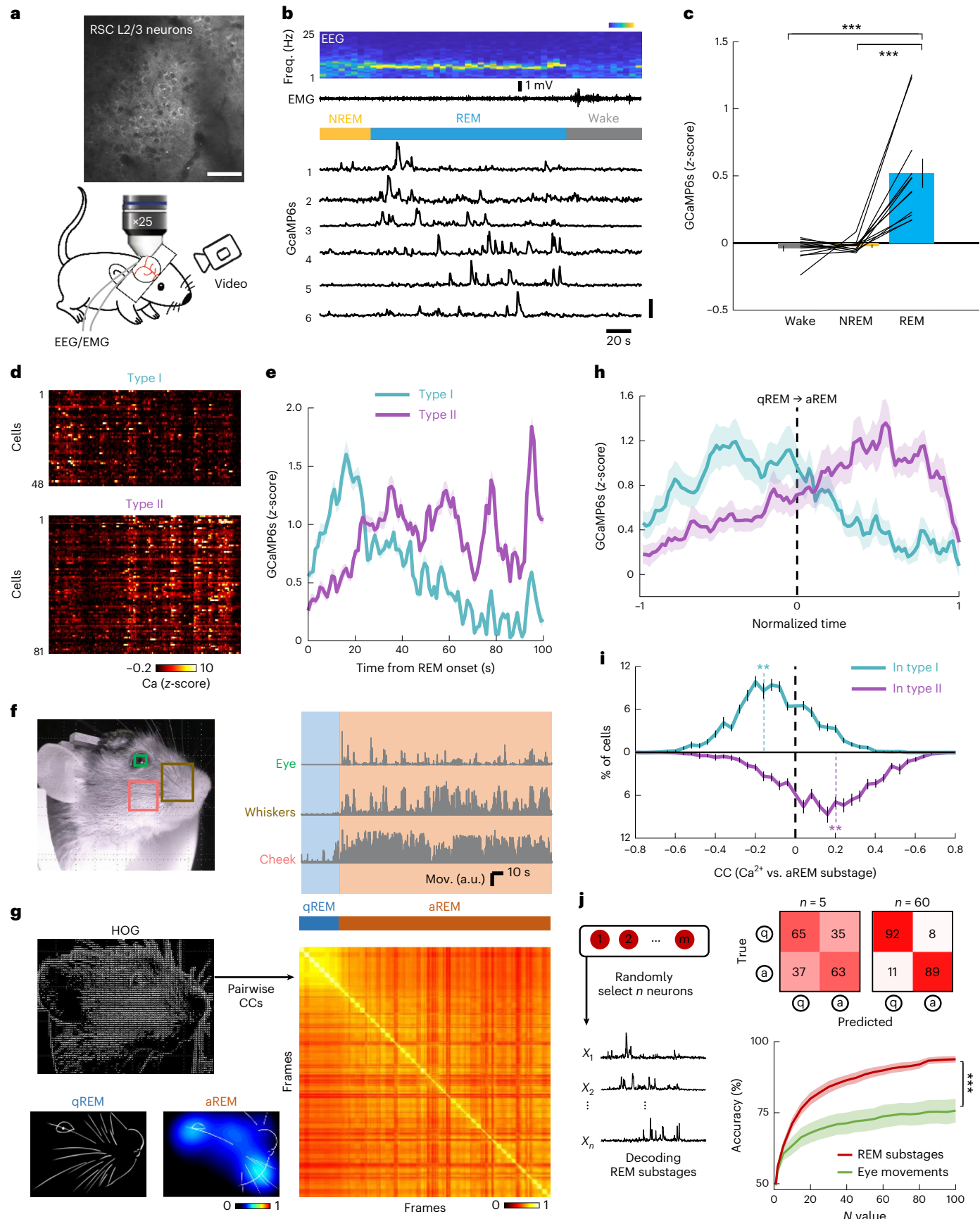
To achieve high inhibition efficiency for behavioral measurements, we next injected RSC L2/3 bilaterally with AAV expressing light-gated chlorine channel GtACR2 (AAV-CaMKIIα-GtACR2-EGFP)²⁹, which could be efficiently activated by blue light (Supplementary Fig. 5). Here we used an online sleep scoring method to achieve REM sleep-specific light delivery: light was initiated within 10 s after REM sleep onset and maintained throughout the REM episode (Fig. 4f, Supplementary Fig. 4b–d and Methods). The durations of qREM, aREM and total REM were compared between mice with RSC_{REM} inactivation and GtACR2-expressing mice without RSC_{REM} inactivation (‘GtACR2 control’) or mice with light stimulation but no GtACR2 expression (‘light control’). We found that

Fig. 3 | RSC L2/3 neuronal population activity encodes two REM sleep substages. **a**, Schematic for two-photon imaging of RSC L2/3 neurons.

b, Example calcium traces of RSC L2/3 neurons together with EEG spectrogram, EMG trace and brain states. The vertical line indicates 10 $\Delta F/F$. **c**, Average calcium activity of RSC populations across sleep states. Each line indicates averaged activity for all identified neurons from one recording session ($n = 12$ sessions from 6 mice). *** $P < 0.001$, two-sided paired t -test. **d**, Calcium activity for two types of REM-active neurons in the RSC L2/3 during an example REM episode. **e**, Averaged type I and II calcium activity during REM sleep across sessions ($n = 12$). **f**, Example image and trace from a video recording showing movements of the eye, whiskers and cheek. a.u., arbitrary units. **g**, Automated classification of REM substages. Pairwise CC matrix for HOGs of video frames in **f**. The two clusters correspond to qREM and aREM substages. In the heat map, the color

shows the difference between qREM or aREM with NREM sleep at each pixel.

h, Averaged type I and type II activity aligned with the qREM → aREM transition ($n = 27$ REM sleep episodes). Time was normalized to qREM or aREM duration. The vertical dashed line indicates the transition point. **i**, Distribution of CC (Ca^{2+} activity versus aREM) in type I ($n = 38$ neurons per episode) and type II ($n = 48$ neurons per episode) RSC populations. The distribution was calculated for each episode before averaging across 27 REM episodes. Cyan/purple vertical lines represent mean CCs. ** $P_{\text{TypeI}} = 0.0036$, ** $P_{\text{TypeII}} = 0.0097$, compared to zero, one-tailed z -test. **j**, Schematic showing population decoding of REM substages. Confusion matrices for decoding REM substages by activity of $n = 5$ or 60 neurons. Prediction accuracy for decoding REM substages or eye movements ($n = 12$ sessions). *** $P < 0.0001$, two-way ANOVA test. Bars and shadings indicate the s.e.m.



RSC_{REM} inactivation markedly reduced the duration of aREM sleep (27.96 ± 3.78 s in RSC_{REM} inactivation; 104.50 ± 14.25 s in GtACR2 control; 70.64 ± 8.79 s in light control; $P < 0.00001$ for comparisons with controls) and increased the duration of qREM sleep (43.60 ± 3.07 s in RSC_{REM} inactivation; 20.50 ± 2.96 s in GtACR2 control; 22.91 ± 2.76 s in light control; $P < 0.00001$ for comparisons with controls), resulting in a shortening of total REM duration ($P < 0.05$; Fig. 4*h,i*, Extended Data Fig. 8a–d and Supplementary Video 2). This effect of RSC_{REM} inactivation was largely due to the inhibition of qREM-to-aREM transitions ($P < 0.0001$), rather than simply the induction of wakefulness (Fig. 4*j*), indicating that aREM initiation is crucial for maintaining REM sleep. RSC neurons were also important for aREM sleep maintenance, as RSC_{aREM} inactivation largely reduced aREM duration ($P < 0.0001$; Extended Data Fig. 8e–h). Moreover, during the 4-h recording sessions with RSC_{REM} inactivation, the average number of REM episodes was increased as compared to that found in control mice (Fig. 4*j*). This may be attributed to REM sleep pressure resulting from REM sleep disruption.

We also tested the effect of RSC inactivation during NREM sleep (Extended Data Fig. 8i,j). Light stimulation lasting for 1 min was delivered to the RSC of GtACR2-expressing mice or control mice. No difference were found between the generation of either wakefulness or REM sleep and NREM sleep between the two groups ($P > 0.8$, bootstrap test; Extended Data Fig. 8j), indicating that RSC inactivation during NREM sleep did not promote NREM \rightarrow REM or NREM \rightarrow wake transition. Furthermore, we performed closed-loop inactivation of the M2 or ACC excitatory neurons during REM sleep. We found that neither M2_{REM} inactivation nor ACC_{REM} inactivation altered the duration of the two REM substages or the total REM episode (Extended Data Fig. 9; $P > 0.4$ in all comparisons for M2, and $P > 0.05$ for ACC). Finally, we performed retrograde tracing from RSC or M2 to compare their upstream inputs and found that RSC preferentially received strong inputs from REM sleep-related brain areas, such as the hippocampal subiculum³⁰ and the lateral pontine area³ (Extended Data Fig. 10). Taken together, our results showed that RSC is not only a mediator of cortical waves, but is also actively involved in regulating substage transition during REM sleep.

Discussion

In this study, we have shown that the RSC is activated and initiates propagating activity waves to V1 and ACC during REM sleep (Figs. 1 and 2). This RSC activation is consistent with previous findings that the rat RSC showed enhanced cFos activity during sleep after REM sleep deprivation^{23,31} and exhibited higher firing activity even compared to the active wake state³². Previous human studies also showed that the posterior cortices (including visual areas) and limbic cortices (including ACC) were activated during REM sleep³³, potentially relating to visual hallucination and emotional content during vivid dreaming¹³. Our results indicate that in head-fixed mice, such patterned cortical activation is likely mediated at least in part by the RSC (Fig. 4a–e). It is important to note that further studies are needed to establish whether these RSC-initiated cortical waves also occur during natural REM sleep in freely moving animals.

Fig. 4 | RSC activity is required for substage transition during REM sleep. **a**, Schematics showing concurrent optogenetic inactivation and wide-field Ca²⁺ imaging. **b**, Averaged RSC calcium activity between control ($n = 6$ sessions from 5 mice) and RSC_{REM} inactivation ($n = 6$ sessions from 4 mice) groups. The vertical line indicates the transition point. $***P < 0.0001$ for comparison of activity during REM, bootstrap test for 10,000 iterations. Shading indicates the s.e.m. **c**, Difference of cortex-wide average activity between RSC_{REM} inactivation and control across sleep states. **d**, Occurrence probability of seven common motifs between control and RSC_{REM} inactivation groups across sleep states. **e**, Differences of occurrence probability between control and RSC_{REM} inactivation groups across sleep states. The hash symbol indicates a decrease at $P < 0.05$, two-sided unpaired *t*-test. **f**, Schematic of closed-loop optogenetics stimulation

We show that upstream inputs to the RSC were widely distributed in the brain (Extended Data Fig. 10). It has been reported that neurons in the claustrum projecting to the RSC are also active during REM sleep hypersomnia^{23,31}, suggesting that the claustrum may be involved in activating RSC during REM sleep. RSC receives strong inputs from the retrohippocampal region, particularly the dorsal subiculum, whose activation was reported to be theta phase-locked during REM sleep³⁴. Such direct connection could provide an anatomical basis for the synchrony of RSC neuronal spiking with hippocampal theta waves, which may be essential for REM sleep-dependent memory consolidation^{30,32}. In addition, RSC receives direct inputs from the peri-locus coeruleus region in the lateral pontine area, which is reported to be involved in REM sleep regulation³. Moreover, studies also showed that different types of local microcircuits differentially modulated the activity of pyramidal neurons in the cortex during REM sleep¹⁷. Given that RSC L2/3 and L5 pyramidal neurons exhibited opposite activity during REM sleep (Extended Data Fig. 3), it will be important to examine how these neurons integrate information from multiple long-range inputs as well as local microcircuits.

Studies into the function of REM sleep functions have revealed inconsistent findings^{25,35,36}, possibly because of the heterogeneous nature of REM sleep. In this study, we discovered two distinct sequential substages of REM in mice—qREM and aREM (Fig. 3 and Extended Data Figs. 5 and 6). Despite skeleton muscle atonia throughout REM sleep, mice exhibited enriched facial movements during the aREM substage. This is also consistent with the observation of interleaved eye movements and facial muscle contractions during human REM sleep^{25,37}. The two REM substages exhibited distinct patterns of EEG theta oscillations, with qREM associated with low theta oscillations and aREM associated with high theta oscillations. Previous studies have revealed two similar types of theta oscillations during wake periods^{38,39}, with low theta oscillations occurring during immobility and emotional states and high theta occurring during exploration. Whether the two types of EEG theta oscillations in qREM and aREM are linked to distinct functions of REM sleep (for example, emotion processing or memory consolidation) remains to be explored.

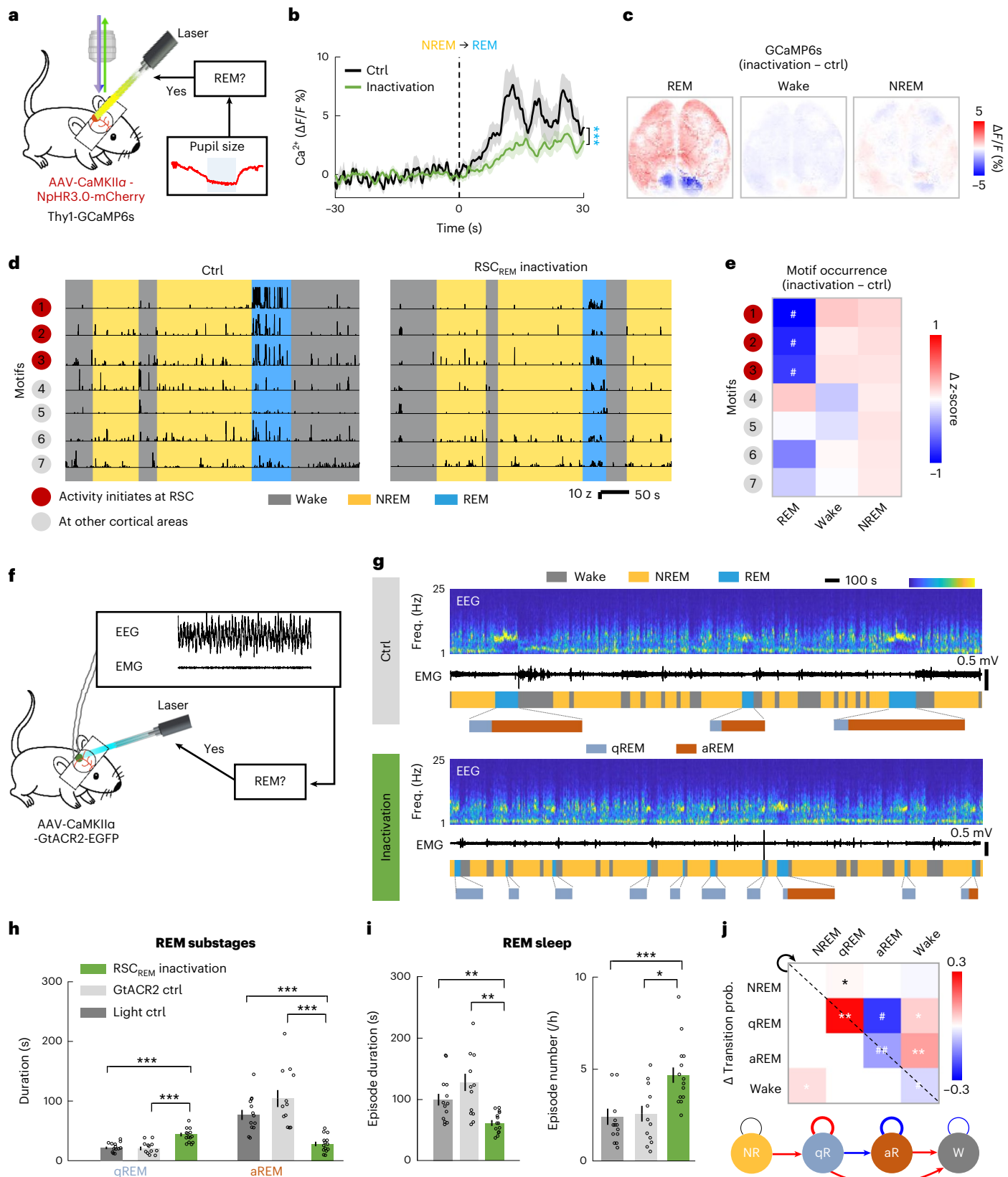
Importantly, we found two RSC neuronal populations encoding information associated with the two REM substages (Fig. 3). The two types of activity could be differentially involved in REM substage regulation. The type I and type II neurons were active in qREM and aREM, respectively (Fig. 3*h,i*). Inactivation of RSC L2/3 neurons largely inhibited the qREM \rightarrow aREM transition and aREM maintenance (Fig. 4*f–j* and Extended Data Fig. 8). This could imply that the type I activation during qREM may be essential for substage transition and type II activation is important for the maintenance of aREM. Although many neurons showed dynamic activation across REM sleep episode, the number of neurons that are constantly active at a certain substage was significantly higher than random control (Extended Data Fig. 4*e*), suggesting that small subsets of neurons dynamically recruit RSC populations to encode the two REM substages. Identifying and labeling these subsets for recording and manipulation is required to test their causal role in REM sleep regulation. Finally, further studies

for behavioral measurements. **g**, Example EEG spectrogram, EMG trace, brain states and REM substages in GtACR2 control and RSC_{REM} inactivation groups. **h**, Duration of qREM and aREM in three groups: light control, YFP/mCherry-expressing mice with light stimulation ($n = 13$ sessions from 9 mice); GtACR2 control ($n = 12$ sessions from 6 mice), GtACR2-expressing mice without light; and RSC_{REM} inactivation ($n = 14$ sessions from 7 mice). Each point represents one recording session. **i**, Average duration and episode number of total REM sleep during 4-h recordings. $*P < 0.05$, $**P < 0.01$, $***P < 0.001$, two-sided unpaired *t*-test. Error bars denote the s.e.m. **j**, RSC_{REM} inactivation-induced changes in transition probability. The increase transition from wake (W) to NREM (NR) is not shown in the summary plot (bottom). $*/\#$, increase/decrease, $P < 0.05$; $**/\#$, increase/decrease, $P < 0.0005$, one-sided unpaired *t*-test.

on the circuit mechanism underlying the activity dynamics of RSC neurons and their differential roles in initiating REM-associated cortical waves will help to elucidate the complexity of REM regulation and their physiological functions.

Online content

Any methods, additional references, Nature Portfolio reporting summaries, source data, extended data, supplementary information, acknowledgements, peer review information; details of author contributions



and competing interests; and statements of data and code availability are available at <https://doi.org/10.1038/s41593-022-01195-2>.

References

1. Scammell, T. E., Arrigoni, E. & Lipton, J. O. Neural circuitry of wakefulness and sleep. *Neuron* **93**, 747–765 (2017).
2. Liu, D. & Dan, Y. A motor theory of sleep–wake control: arousal–action circuit. *Annu. Rev. Neurosci.* **42**, 27–46 (2019).
3. Lu, J., Sherman, D., Devor, M. & Saper, C. B. A putative flip-flop switch for control of REM sleep. *Nature* **441**, 589–594 (2006).
4. Weber, F. et al. Control of REM sleep by ventral medulla GABAergic neurons. *Nature* **526**, 435–438 (2015).
5. Sanchez-Vives, M. V. & McCormick, D. A. Cellular and network mechanisms of rhythmic recurrent activity in neocortex. *Nat. Neurosci.* **3**, 1027–1034 (2000).
6. Funk, C. M., Honjoh, S., Rodriguez, A. V., Cirelli, C. & Tononi, G. Local slow waves in superficial layers of primary cortical areas during REM sleep. *Curr. Biol.* **26**, 396–403 (2016).
7. Valero, M. et al. Sleep down state-active ID2/NKx2.1 interneurons in the neocortex. *Nat. Neurosci.* **24**, 401–411 (2021).
8. Vyazovskiy, V. V. & Harris, K. D. Sleep and the single neuron: the role of global slow oscillations in individual cell rest. *Nat. Rev. Neurosci.* **14**, 443–451 (2013).
9. Krone, L. B. et al. A role for the cortex in sleep–wake regulation. *Nat. Neurosci.* **24**, 1210–1215 (2021).
10. Moraity, S. R. et al. A role for cortical nNOS/NK1 neurons in coupling homeostatic sleep drive to EEG slow wave activity. *Proc. Natl Acad. Sci. USA* **110**, 20272–20277 (2013).
11. Aserinsky, E. & Kleitman, N. Regularly occurring periods of eye motility, and concomitant phenomena, during sleep. *Science* **118**, 273–274 (1953).
12. Jouvet, M. Paradoxical sleep—a study of its nature and mechanisms. *Prog. Brain Res.* **18**, 20–62 (1965).
13. Siclari, F. et al. The neural correlates of dreaming. *Nat. Neurosci.* **20**, 872–878 (2017).
14. Cardin, J. A., Crair, M. C. & Higley, M. J. Mesoscopic imaging: shining a wide light on large-scale neural dynamics. *Neuron* **108**, 33–43 (2020).
15. Makino, H. et al. Transformation of cortex-wide emergent properties during motor learning. *Neuron* **94**, 880–890 (2017).
16. Kim, T. H. et al. Long-term optical access to an estimated one million neurons in the live mouse cortex. *Cell Rep.* **17**, 3385–3394 (2016).
17. Aime, M. et al. Paradoxical somatodendritic decoupling supports cortical plasticity during REM sleep. *Science* **376**, 724–730 (2022).
18. Yuzgec, O., Prsa, M., Zimmermann, R. & Huber, D. Pupil size coupling to cortical states protects the stability of deep sleep via parasympathetic modulation. *Curr. Biol.* **28**, 392–400 (2018).
19. Reidl, J., Starke, J., Omer, D. B., Grinvald, A. & Spors, H. Independent component analysis of high-resolution imaging data identifies distinct functional domains. *Neuroimage* **34**, 94–108 (2007).
20. Barnett, L. & Seth, A. K. The MVGC multivariate Granger causality toolbox: a new approach to Granger-causal inference. *J. Neurosci. Methods* **223**, 50–68 (2014).
21. MacDowell, C. J. & Buschman, T. J. Low-dimensional spatiotemporal dynamics underlie cortex-wide neural activity. *Curr. Biol.* **30**, 2665–2680 (2020).
22. Mackevicius, E. L. et al. Unsupervised discovery of temporal sequences in high-dimensional datasets, with applications to neuroscience. *Elife* <https://doi.org/10.7554/elife.38471> (2019).
23. Maciel, R. et al. Is REM sleep a paradoxical state?: Different neurons are activated in the cingulate cortices and the claustrum during wakefulness and paradoxical sleep hypersomnia. *Biochem. Pharmacol.* **191**, 114514 (2021).
24. Dolensek, N., Gehrlach, D. A., Klein, A. S. & Gogolla, N. Facial expressions of emotion states and their neuronal correlates in mice. *Science* **368**, 89–94 (2020).
25. Simor, P., van der Wijk, G., Nobili, L. & Peigneux, P. The microstructure of REM sleep: why phasic and tonic? *Sleep. Med. Rev.* **52**, 101305 (2020).
26. Koroma, M. et al. Sleepers selectively suppress informative inputs during rapid eye movements. *Curr. Biol.* **30**, 2411–2417 (2020).
27. Patel, A. K., Reddy, V. & Araujo, J. F. *Physiology, Sleep Stages* (StatPearls, 2022).
28. Hong, C. C. et al. fMRI evidence for multisensory recruitment associated with rapid eye movements during sleep. *Hum. Brain Mapp.* **30**, 1705–1722 (2009).
29. Mahn, M. et al. High-efficiency optogenetic silencing with soma-targeted anion-conducting channelrhodopsins. *Nat. Commun.* **9**, 4125 (2018).
30. de Almeida-Filho, D. G. et al. Hippocampus–retrosplenial cortex interaction is increased during phasic REM and contributes to memory consolidation. *Sci. Rep.* **11**, 13078 (2021).
31. Renouard, L. et al. The supramammillary nucleus and the claustrum activate the cortex during REM sleep. *Sci. Adv.* **1**, e1400177 (2015).
32. Koike, B. D. V. et al. Electrophysiological evidence that the retrosplenial cortex displays a strong and specific activation phased with hippocampal theta during paradoxical (REM) sleep. *J. Neurosci.* **37**, 8003–8013 (2017).
33. Braun, A. R. et al. Regional cerebral blood flow throughout the sleep–wake cycle. An $H_2^{15}O$ PET study. *Brain* **120**, 1173–1197 (1997).
34. Kitanishi, T., Umaba, R. & Mizuseki, K. Robust information routing by dorsal subiculum neurons. *Sci. Adv.* <https://doi.org/10.1126/sciadv.abf1913> (2021).
35. Rasch, B. & Born, J. About sleep’s role in memory. *Physiol. Rev.* **93**, 681–766 (2013).
36. Walker, M. P. The role of sleep in cognition and emotion. *Ann. N. Y. Acad. Sci.* **1156**, 168–197 (2009).
37. Rivera-Garcia, A. P., Ramirez-Salado, I., Corsi-Cabrera, M. & Calvo, J. M. Facial muscle activation during sleep and its relation to the rapid eye movements of REM sleep. *J. Sleep. Res.* **20**, 82–91 (2011).
38. Mikulovic, S. et al. Ventral hippocampal OLM cells control type 2 theta oscillations and response to predator odor. *Nat. Commun.* **9**, 3638 (2018).
39. Goyal, A. et al. Functionally distinct high and low theta oscillations in the human hippocampus. *Nat. Commun.* **11**, 2469 (2020).

Publisher’s note Springer Nature remains neutral with regard to jurisdictional claims in published maps and institutional affiliations.

Springer Nature or its licensor (e.g. a society or other partner) holds exclusive rights to this article under a publishing agreement with the author(s) or other rightsholder(s); author self-archiving of the accepted manuscript version of this article is solely governed by the terms of such publishing agreement and applicable law.

© The Author(s), under exclusive licence to Springer Nature America, Inc. 2022

Methods

Animals

All procedures were approved by the Animal Care and Use Committees of the Center for Excellence in Brain Science and Intelligence Technology, Chinese Academy of Sciences. Wide-field imaging, two-photon imaging of RSC L2/3 and fiber photometry experiments were performed on *Thy1*-GCaMP6s mice (GP4.3Dkim, Jackson Laboratory stock, 024275); two-photon imaging of RSC L5 neurons was performed on *Rbp4*^{Cre} mice (Mutant Mouse Resource and Research Center, 031125); optogenetic experiments were performed on *CaMKIIα*^{Cre} (005359) and C57BL/6 mice. Adult (aged 2–6 months) male and female mice were used for all experiments. Mice were housed under standardized conditions with a 12 h–12 h light–dark cycle, with the temperature controlled at 22–23 °C and humidity at 40–70%. Recordings were performed during the light phase, and each recording session lasted for <4 h, from 10:00 to 14:00 or 14:00 to 18:00. Female and male mice were randomly assigned to each experimental group. For optogenetic experiments, mice from the same cage were randomly assigned to the inactivation or light control group; the sequence of inactivation or GtACR2 control sessions was randomized. For comparison of sleep under head-fixed or freely moving conditions, mice were randomly assigned to groups with head-fixed sleep recording on the first day and freely moving sleep recording on the second day, or vice versa.

Surgical procedures

Adult mice were anesthetized with 1.5–2% isoflurane and placed on a stereotaxic frame. Body temperature was kept stable throughout the procedure using a heating pad. To minimize brain edema, we injected dexamethasone (32 mg per kg body weight) subcutaneously before surgical incision. We applied ointment to the mouse's eyes to maintain their moisture. After asepsis, the skin was incised to expose the skull, and the overlying connective tissue was removed.

For wide-field Ca²⁺ imaging. As previously described¹⁶, the margin of the skull of whole dorsal cortex that matched the trapezoidal glass implant was carefully thinned by a 0.5-mm drill. During the drilling, we repeatedly perfused saline and checked the thickness of the bone integrity. After disconnecting the bone from the surrounding skull and tissues, we carefully removed the skull and covered it with the glass window. We pressed the window gently to ensure the skull made contact with the cortical surface. We applied tissue adhesive (3 M) to seal the window and secured the window to remaining skull using dental cement.

Two-photon imaging and optogenetic inactivation. A region of skull with the diameter at -3 mm over targeted cortical regions was removed, exposing the dura. A custom-made double-layered cover glass was used to cover the cortex. Tissue adhesives (3 M) and dental acrylic were used to seal the cover glass.

Fiber photometry. Optical fibers (200-μm core, 0.37 NA, 1.25-mm ferrule, Inper) were implanted into the RSCs, the RSCg, the ACCg and the posterior insula cortex of the same *Thy1*-GCaMP6s mice. Light-curing adhesive (SO307258, CharmFil Flow) and dental acrylic were used to fix the fibers.

Viral/tracer injection. A craniotomy (0.5–1 mm diameter) was made, and 0.2–0.5 μl AAV9-hSyn-DIO-GCaMP6s, AAV9-CaMKIIα-NPHR3.0-mCherry, AAV9-hSyn-DIO-GtACR2-EGFP, AAV9-CaMKIIα-GtACR2-EGFP, AAV9-CaMKIIα-mCherry or AAV9-CaMKIIα-EYFP was injected bilaterally into the RSC, ACC or M2. For the inactivation efficiency test of GtACR2, 0.15 μl AAV-CaMKIIα-GtACR2 and 0.15 μl AAV-hSyn-jRCECO1a were co-injected into L2/3 of the RSC. These viruses were purchased from Braincase or Taitool. For retrograde tracing, 0.3 μl red retrobeads (Lumafluor)

or CTB-647 (Invitrogen) was injected unilaterally into the RSC or M2. Virus/tracer was injected using Nanoject III (Drummond Scientific) via a glass micropipette with a tip diameter of 15–20 μm.

Stereotaxic coordinates for injection/implantation were:

RSC L2/3: bregma (AP, -3.0 mm; ML, 0.45 mm; DV (from cortical surface), 0.5 mm);

RSC L5: AP, -3.0 mm; ML, 0.45 mm; DV, 0.7 mm;

RSCg: AP, -2.8 mm; ML, 0.4 mm; DV, 1.0 mm;

M2: AP, +0.45 mm; ML, 0.6 mm; DV, 0.6 mm;

ACCg: AP, +1.0 mm; ML, 0.4 mm; DV, 1.2 mm;

Insula cortex: AP, -0.45 mm; ML, 4.05 mm; DV, 2.7 mm.

EEG and neck EMG recording. To implant EEG and EMG recording electrodes, one stainless-steel screw was inserted into the skull 1.5 mm from the midline and 1.5 mm anterior to bregma. For wide-field imaging mice, one EEG electrode was inserted into the skull on top of the auditory cortex to expose the whole dorsal cortex for imaging. Two EMG electrodes were inserted into the neck musculature. A reference screw was inserted into the skull on top of the right cerebellum. Insulated leads from the EEG and EMG electrodes were soldered to a pin header, which was secured to the skull using dental cement. A custom-made stainless-steel headplate with a screw hole was embedded into the dental acrylic for head-fixed recording.

Facial EMG recording. To record facial movements in freely moving mice, the skin of the cheek was shaved and cut to expose the masseter. The bare wire passed through the temporal muscle and then hooked into the masseter muscle⁴⁰. Tissue adhesive (3 M) was used to fix the wire in the place. Skin was sutured and the insulating part of the wire was held in place by dental cement.

After surgery, mice returned to the home cage with wet food pellets and hydrogel provided. Glucose (5%) and sodium chloride (0.9%) was injected (200 μl per mouse) intraperitoneally for 3 d. Ceftriaxone sodium (200 mg per kg body weight) was injected for 3 d after surgery to prevent inflammation. Mice were allowed to recover for at least 2 weeks before recording.

Habituation for head-fixed sleep

After recovery from surgery, mice were first habituated under the head-fixed condition. Mice were head-fixed with body in a tube. We habituated each mouse once per day, and the time increased gradually over habituation session (from 2 to 4 h). For the first session, the habituation time was less than 2 h, and mice rarely fell into sleep. The latency to fall asleep decreased with training. Normally, after ~1 week of habituation, the average sleep onset was ~30–60 min (Supplementary Fig. 1). Mice that did not show signs of sleep within the first 2 h during habituation sessions did not progress to the next stage of experiments. For imaging experiments, mice were habituated under the microscope in the dark.

Behavioral and sleep recording

Mouse facial behavior was recorded using a 940-nm infrared video camera (custom made) focusing on the mouse face at 30 frames per second (f.p.s.), along with EEG and EMG recordings. EEG and EMG electrodes were connected to flexible recording cables via a mini-connector. Recordings started after 30 min of habituation for each session. For most sleep recordings, EEG and EMG signals were recorded with an Open Ephys system, filtered (>0.5 Hz) and digitized at 1,000 Hz. For closed-loop optogenetic stimulation experiments, EEG and EMG signals were recorded and amplified with Medusa Server (Bio-Signal) at 500 Hz and communicated in real time to MATLAB using the UDP protocol. In MATLAB, the signals were collected and filtered (high-pass filter, over 1 Hz; band-stop filter, 50 Hz) in every 2.5 s for online sleep scoring. For EEG and EMG recording in freely moving mice, the signals were recorded with a TDT RZ5 amplifier, filtered (1–300 Hz) and digitized at 1,000 Hz.

Behavior and sleep analysis

Sleep-wake scoring. For offline sleep scoring, spectral analysis was carried out using fast Fourier transform, and brain states were classified into wake (wake: low delta (1–4.5 Hz) power, low theta-to-delta ratio (6–10 Hz); aWake: high neck EMG power and high facial movements; qWake: low facial movements) and sleep states (NREM, synchronized EEG with high delta power and low neck EMG power; REM, high theta-to-delta ratio, low neck EMG power), with an epoch length of 5 s. For REM sleep onset, we also carefully inspected the EEG/EMG data with a 1-s temporal resolution, and the time point when theta-to-delta ratio sharply increased to more than one standard deviation from its mean was determined as the REM sleep onset. The classification was made using a custom-written graphical user interface⁴¹.

For real-time sleep scoring, we modified the open-source Sleep Scoring Artificial Neural Network and the graphic interface from Barger et al.⁴¹ for real-time classification, and visualization of the EEG, EMG and annotated brain states. To decrease latency for closed-loop feedback, the epoch length here was 2.5 s. We called the trained Sleep Scoring Artificial Neural Network in real time to score the brain states based on the standardized joint EEG/EMG spectrogram of the current together with the eight most recent epochs (22.5 s). Based on the scoring result of the latest epoch, the MATLAB output was refreshed to regulate the onset laser stimuli every 2.5 s.

Behavior and REM substage analysis. Facial movement analysis. Offline facial behavior analysis was processed using custom MATLAB scripts. For analysis of pupils, we used Ostu's method to find a proper threshold to extract pupils with noise as less as possible for each recording session. As pupil movements were shown to correlate with eye movements in mice⁴², we thus used pupil movements that were easily measured from mouse facial video recordings to monitor eye movements during REM sleep. Eye movements were measured by calculating changes in center of mass of the pupil, frame by frame. The pupil radius was calculated by averaging the length and width of the maximum bounding box for each frame. For whisker and cheek movement analysis, temporal difference analysis with Ostu's method (MATLAB function graythresh) was performed. For online analysis of pupil size, a facial video was recorded at 25 f.p.s. using open-source software Bonsai. Images of eye areas were cropped, thresholded and binarized. Similarly to offline analysis, the radius of the pupil in each frame was measured in real time. Once the pupil radius was less than a preset criterion, an 'on' signal was sent to an Arduino board.

REM substage analysis based on facial movements. Based on a previous study of facial expression analysis²⁴, we used HOGs for mouse feature description. The algorithm counts occurrences of gradient orientation in localized portions of an image. HOG descriptors for each video frame were created using the following parameters: eight histogram orientation bins, using square cells with a height of 32 pixels and one cell per block, with images cropped as shown in Fig. 3f.

Following conversion of each video frame of REM episode into a HOG vector, pairwise CC analysis was performed and formed a similarity matrix (Fig. 3g). After hierarchical clustering for CCs, there are two distinct classes: one has highly uniform CCs representing few facial movements, while the other has variable CCs representing enriched facial movement. The two clusters were defined as qREM and aREM, corresponding to behavioral states without any movements, and with enriched facial and eye movements, respectively. Every REM episode was treated in the same way. Poor-quality video recordings were not used for this analysis. For freely moving mice, aREM was defined by the periods with high facial EMG power during REM sleep, and qREM was defined as REM sleep periods with low facial EMG power.

Heart rate variability and respiration rate analysis. We analyzed electrocardiogram from EMG signals. Inter-beat (RR) intervals were

detected by findpeaks function in MATLAB with following parameters: MinPeakDistance, 62; MinPeakHeight, 150. Heart rate variability was calculated using an open-source MATLAB toolbox: HRVTool version 1.04 with rrHRV method⁴³ (<https://marcusvollmer.github.io/HRV/>). We calculated the respiration rate from the chest expansion movement in video recordings manually.

Optogenetics inactivation

Inactivation efficiency test of GtACR2. AAV-CaMKIIα-GtACR2 and AAV-hSyn-jRGECO1a were co-injected into the L2/3 of the RSC. After 2 weeks of virus expression, a chronic window was implanted above the RSC, to monitor the neuronal activity. We recorded the jRGECO1a signal⁴⁴ (excited by green light at 550 nm) using the wide-field microscope and delivered blue light (470 nm at 2 mw/mm²) lasting for 60 s or 30 s randomly at an interval of 7–10 min. Each recording session lasted for less than 30 min.

Closed-loop optogenetic inactivation. The closed-loop light stimulation system is controlled by the microcontroller Arduino. As pupil size was shown to decrease at few seconds before entering REM¹⁸, we first established a pupil size-based closed-loop system to predict REM sleep. An 'on' signal was sent by Bonsai to an Arduino board when pupil size was less than a certain threshold (manually calibrated for each mouse), and otherwise an 'off' signal was sent by Bonsai. For the sleep scoring-based closed-loop system, detection of two consecutive REM epochs triggered an 'on' signal from MATLAB to an Arduino board, whereas detection of one wake or NREM epoch triggered an 'off' signal. For aREM-specific inactivation experiments, we set a 25 s delay for sending out 'on' signal once detecting REM sleep state. The onset of light stimulation in the two closed-loop systems was different: with light starting at -30 s before REM initiation in the pupil size-based system, and at -7.5 s after REM initiation in the sleep scoring-based system (Supplementary Fig. 4). In both systems, the light was constantly on throughout the REM episode. Each recording session lasted for ~4 h, and each mouse was tested for 2–3 sessions.

We implemented an Arduino code to convert the 'on' or 'off' signal to a high or low voltage TTL output to trigger a laser. For GtACR2 inactivation, an optic fiber, which was attached through an FC/PC adaptor to a 473-nm blue laser diode (Shanghai laser), was fixed above the transparent window at the RSC. We made sure that the light covered the whole RSC at an average light power of ~2 mW/mm². For concurrent NpHR-mediated optogenetic inactivation and wide-field imaging, an optical fiber was attached to a 593-nm yellow laser diode (Shanghai laser), fixed on a platform ~30 cm away from the mouse brain. The laser was delivered peculiarly to the RSC through a plano-convex lens (350 nm–2.0 μm, N-BK7 Plano-Convex Lenses, ThorLabs), and light power on the surface of RSC was at ~7 mW/mm².

For optogenetic inactivation during NREM sleep, constant light (~2 mW/mm²) lasting for 60 s was delivered to the RSC through a chronic window at a random interval of 7–20 min. Trials in which mice were in NREM sleep before laser onset were included for analyzing the effect of RSC inactivation during NREM sleep.

Multi-site fiber photometry recording

Ten days after fiber implantation, mice were recorded by a four-channel fiber photometry system (FP-3001, Neurophotometrics), together with EEG/EMG recordings. A four-channel fiber-optic patch cord (200-μm core, 0.37 NA, 1.25 mm ferrule, low autofluorescence; Doric) was attached to the mouse's fiber implants using ceramic split-sleeves. Interleaved 470 nm and 405 nm lasers, at a power of 20–40 μw, were emitted at 10 f.p.s. for each wavelength. Signals were collected by Bonsai (version 2.3). Each recording session was triggered by a TTL signal from the TdT RZ5 system for alignment with EEG/EMG signals.

Two-photon Ca^{2+} imaging

Head-fixed two-photon imaging was performed with a two-photon microscope (Sutter) controlled by ScanImage (Janelia). The objective used was $\times 25$, 1.05 NA (Olympus). A digital zoom of 1–2 was used. A Ti:sapphire laser (Spectra Physics) was used as the light source and tuned to 920 nm for imaging. Image sequences were taken at layer 2/3, 200–300 μm deep from the cortical surface. Imaging started after mice fell asleep under the head-fixed condition (~30–60 min after setting up). Each imaging session lasted for ~1–2 h. Imaging, behavioral video and sleep recording were acquired simultaneously and aligned offline based on the synchronization signal.

Cortex-wide Ca^{2+} imaging with multi-wavelength excitation

Wide-field calcium imaging was performed using a commercial fluorescence microscope (MVX10, Olympus, $\times 1$ objective). Imaging started after mice fell asleep under the head-fixed condition (~30–60 min after setting up). Each imaging session lasted for ~1–2 h. A CMOS camera (Moment, 7 MP, 17.5 mm sensor diagonal, 50 f.p.s.) was used to record fluorescence signals, with a 535/45 (Chroma) emission filter. CoolLED pE-300 ultra-illumination system was used to deliver excitation light. Alternating 470 nm (91 $\mu\text{W}/\text{mm}^2$) and 410 nm (87 $\mu\text{W}/\text{mm}^2$) illumination was delivered for hemodynamic artifact removal. The light alternation was controlled using a custom-made streaming system slaved to the frame output trigger of the camera. Images were acquired using Micro-Manager at 1,024 \times 1,024 pixels (field of view, 11 mm \times 11 mm; binning, 2; 16 bit), at an exposure time of 20 ms. The output trigger from the camera was also recorded by the Open Ephys system using Bonsai for data synchronization. Imaging, behavioral video and sleep recording were acquired simultaneously and aligned offline based on the synchronization signal.

Histology

Mice were deeply anesthetized and transcardially perfused with 0.1 M PBS followed by 4% paraformaldehyde in PBS. Brains were kept overnight in 4% paraformaldehyde for fixation. For cryoprotection, brains were placed in 30% sucrose in PBS solution for 36–48 h. After embedding and freezing, brains were sectioned into 40- μm coronal slices using a cryostat (Leica). For detecting viral expression or retrograde input mapping, one of every four sections was imaged using a fluorescence microscope (Olympus VS120, $\times 10$ objective).

Quantification for retrograde tracing

Whole-brain mapping of retrograde-labeled neurons (also referred to as ‘inputs’) was performed as previously described⁴⁵. An automated method for calibrated single-neuron mapping (AMaSiNe; <https://github.com/vsnn-lab/AMaSiNe/>)⁴⁶ was adopted for quantification and three-dimensional (3D) reconstruction of inputs to the M2 and the RSC (three pairs of experiments). This method automatically calibrates the 3D alignment angles of each brain slice to match the standardized 3D Allen Mouse Brain Atlas and assign the position of each neuron in the atlas (<https://mouse.brain-map.org/>), which enables precise comparison of data from multiple brains on a common brain atlas. The number of detected neurons in each region was then divided by the total number of detected cells in the entire brain (after excluding the region within 1 mm from the injection site). Brain areas were grouped into 20 main structures according to the Allen Mouse Brain Atlas (Extended Data Fig. 10). For each upstream region, the RSC-preferring index was calculated as: (inputs to RSC – inputs to M2)/(inputs to RSC + inputs to M2). Regions showing a higher positive index preferentially project to the RSC as compared to the M2, while regions showing a lower negative index preferentially project to the M2.

Wide-field imaging analysis

Multi-wavelength hemodynamic correction. Rapid alternation of a violet wavelength (400–410 nm) with a blue wavelength (470–490 nm) is a well-established method to correct for unspecific hemodynamic artifacts in single-photon imaging system^{14,15,47}. The excitation by the

violet wavelength reflects hemodynamic absorption caused by changes in blood flow or blood vessel diameters, while the excitation by a blue wavelength contains both Ca^{2+} -dependent GCaMP6s signal and the unspecific hemodynamic absorption. Therefore, by subtracting the 410-nm-excited hemodynamic signals from the 470-nm-excited signals, we obtained Ca^{2+} -dependent signals of GCaMP6s.

We followed a previous study⁴⁷ for hemodynamic correction from the fluorescence data with multi-wavelength excitation. Image sequences of the 410-nm channel and 470-nm channels were first normalized with the $\Delta F/F$ method, using the mean fluorescence intensity for each pixel over the entire time series as F . For each pixel, the 410-nm channel was then temporally smoothed using a moving average (width of 500 ms), followed by regressing onto the 470-nm $\Delta F/F$ signal for the corresponding pixel. The regression coefficients were used to scale the 410-nm channel to the 470-nm channel and subtracted from the 470-nm $\Delta F/F$ signal to produce a corrected signal for each pixel. We used the 410 $\Delta F/F$ signal to calculate brain hemodynamics across states in Extended Data Fig. 5h.

Spatial independent component analysis. Images for analyzing independent modules were downsized to 80 \times 80 pixels. Following a previous study¹³, we first performed principle-component analysis (PCA) to remove noise. In PCA, pixels were considered as variables and the $\Delta F/F \text{Ca}^{2+}$ signals for every pixel were treated as observations. The first 40 principal components were subsequently used for ICA. We used the JADER algorithm for ICA analysis⁴⁸, which decomposed mixed signals into independent components (ICs) by minimizing the mutual information using a series of Givens rotations. Forty ICs were extracted by JADER and were spatially independent (referred to as ‘sICs’). We manually inspected all sICs and removed those with artifacts or low signal.

Activity analysis of cortical modules. To identify common cortical modules across mice, sICs from four mice from the six recording sessions were compared. For each sIC, the $\Delta F/F \text{Ca}^{2+}$ signal was computed as the mean of the pixel values within each IC above a weight threshold of 3. We aligned the sICs with the third edition of the mouse brain atlas by Franklin and Paxinos⁴⁹, because it provided much finer cortical structures and correlated better with the measured sICs, as compared to the Allen Mouse Brain Atlas. We manually inspected the Ca^{2+} traces for sICs within a certain anatomical cortical region and merged those with similar Ca^{2+} dynamics. For example, the bilateral symmetric sICs normally show the same dynamics and would be merged into one cortical module. Two bilateral sICs located at the anterolateral part of the cortex did not correspond to any single anatomically defined brain areas, and they were commonly found in each recording session. They span the lateral part of M1, M2 and FrA cortices, and we simply named them as M1/M2. In all, we defined 11 cortical modules based on the sICA: RSC, V1, PPC, S1BF, S1FL, S1HL, ACC, M1, M2, M1/M2 and FrA. The Ca^{2+} signals were averaged across sICs in each cortical module.

Granger causality analysis. The multivariate Granger causality toolbox (version mvgc_v1.2) was used for Granger causality analysis²⁰ (<https://github.com/SacklerCentre/MVGC1/>). Because the duration of REM sleep and wake varied across episodes, to perform Granger causality over trials (or episodes), we first trimmed the Ca^{2+} activity data. For REM sleep, most recorded episodes were longer than 60 s, so we used the activity data within the first 60 s for each episode. REM episodes with a duration of less than 60 s were not included in this analysis. For the wake state, we used activity data in the 60 s after waking up from REM sleep, so that the trial number was the same as that in REM sleep. We also calculated Granger causality for active wake periods lasting longer than 60 s, late REM (60 s preceding REM offset), early NREM sleep (60 s after NREM sleep onset) or late NREM sleep (60 s before

entering REM sleep). This multivariate Granger causality toolbox computes Granger causality based on vector autoregressive modeling. The number of time lags (model order) was estimated by Akaike information criteria with the maximum set to 20. Pairwise conditional causality was then calculated. The pairwise causality contains directional information: the direction 'from' an X module 'to' a Y module indicated that the activity in the X preceded that in Y. Granger causality values that reached $P < 0.01$ (Granger *F* test) after using the false discovery rate for multiple-comparison correction are shown in Fig. 2a,b and Extended Data Figs. 2a–d and 7e,f.

Motif analysis. We followed a previous study²¹ that used the seqNMF algorithm (MATLAB toolbox from ref. ²²; <https://github.com/FeeLab/seqNMF/>) to find spatiotemporal patterns for wide-field imaging data. This method uses convolutional nonnegative matrix factorization with a penalty term to facilitate discovery of repeating sequences. In brief, this method involves (1) multiple motifs that do not exhibit similar sequences, (2) a single motif that is not temporally split into separate smaller motifs and (3) motifs that are encouraged to be nonoverlapping in time.

We first downsized the imaging stack to 80×80 pixels and converted each image to a $6,400 \times 1$ vector of pixel values. Thus, the image sequences were converted to a $6,400 \times T$ (recording time) matrix. To remove noise, each pixel traces were thresholded at two standard deviations above the mean. This matrix can be factorized into a set of K smaller matrices of size $P \times L$ representing repeated sequences ('motifs'). In our study, the K value was set as 20 (20 motifs) for each recording session, and L was set to 50 frames (2 s, for 25 f.p.s.) or 20 frames (2 s, for 10 f.p.s.). The discovered motif was termed W (a $P \times K \times L$ tensor; Fig. 2e and Extended Data Figs. 2 and 7). Each motif was expressed over time according to a $K \times T$ temporal weighting matrix termed H . The values of W and H were found using a multiplicative update algorithm with over 100 iterations. Motifs found in each recording session were manually inspected and those commonly found were double-checked by two experienced experimenters. To compare the occurrence intensity of each common motif in the sleep or wake state, we normalized the temporal weighting (in H) by z-score and averaged across sessions.

Two-photon imaging analysis

Ca²⁺ activity analysis. We first used NoRMCorre, which can correct for both local and global rigid motion, for motion correction of the two-photon image sequences⁵⁰ (<https://github.com/flatironinstitute/NoRMCorre/>). Next, we implemented a constrained nonnegative matrix factorization algorithm to extract neuronal signals^{51,52} (https://github.com/zhoupc/CNMF_E/). The automated recognized neurons were visually inspected, and those displaying nonneuronal morphology were removed. The calcium traces of each neuron were then normalized using a z-score transformation. Neurons that showed significantly higher or lower activity in REM sleep as compared to other states were defined as REM-active or REM-inactive neurons (Extended Data Fig. 3g–j).

For classification of activity patterns of REM-active RSC neurons during REM sleep on an episode-by-episode basis, we first performed pairwise CC among neuronal pairs, followed by *k*-means clustering. The optimal cluster number was 2, estimated by comparing the sum of squares at different cluster numbers ($k = 1$ to 10). Neurons showing higher activity at the first 30 s within REM sleep were defined as type I, and those showing higher activity at the later REM stage were defined as type II. The identities of each neuron in type I or type II across REM episodes were then compared. The identity of a subset of cells remained unchanged across REM episodes. For each pair of REM episodes, we compared the percentage of neurons with stable identity in the observed data to that estimated from random sampling.

For analyzing averaged population activity at REM substage transition (Fig. 3h), we first calculated the average activity of each type during each episode and aligned with the qREM-to-aREM transition point. Time before (qREM) or after (aREM) was normalized, and z-scored traces after time normalization were averaged across episodes. For distribution of CCs between neuronal activity and aREM sleep or pupil movement, we first calculated the CCs between the z-scored activities of each neuron with the binary labeling of aREM or eye movements and calculated the distribution separately in type I and type II neurons for each REM episode. The distribution for each type was then averaged across REM episodes.

Decoding REM sleep substages. To decode REM substages, we used a SVM classifier. For each recording session, we first concatenated Ca²⁺ activity data from all REM episodes. Before training, 25% data of each substage was held out as a validation dataset for prediction accuracy calculation. As the duration of qREM was shorter than that of aREM, we randomly used the aREM data of the same duration as qREM to ensure equal sampling for the two substates. We randomly selected n neurons (n was set as 1, 2, 5, 10 and 100) from all recorded neurons and trained the SVM classifier using the activity from these n neurons using the MATLAB function fitcsvm ('Standardize', true, 'KernelFunction', 'polynomial', 'KernelScale' and 'auto') with tenfold validation. For each n , we repeated the random selection for 2,000 times. The prediction accuracy was tested on the other 25% testing data for each n . We shuffled the relationship between substage labeling and neuronal activity to generate a shuffle dataset, and the accuracy performance of the shuffle dataset was 50%. To decode REMs, eye movement traces were thresholded and binarized to separate periods with or without pupil movements. We followed similar SVM protocols as those used in decoding REM substates.

Statistics and reproducibility

No statistical methods were used to predetermine sample sizes but our sample sizes are similar to those reported previously^{4,15,17,45}. Data collection and analysis were not performed blind to the conditions of the experiments. Batch and automatic analyses were performed for control and experimental groups, yielding no subjective bias. All representative images of histology reflect a minimum of three biological replicates.

Statistical analysis was performed using MATLAB. Data distribution was assumed to be normal but this was not formally tested. Data are shown as means \pm s.e.m. unless otherwise stated. For pairwise comparison of cortical areas in different states, one-way ANOVA with Tukey's multiple-comparison correction was used. Kruskal–Wallis tests were used for comparing averaged neuronal activity after REM sleep onset with NREM baseline, with Dunn's correction for multiple comparisons. Two-way ANOVA was used for comparison of decoding accuracy for REM substages and eye movements. For optogenetic-induced wake generation or REM sleep generation from NREM sleep, we used a bootstrap test for 10,000 iterations⁴⁵. We used a one-sided z-test for comparison of CC distribution (between neuronal activity and aREM or eye movements) with zero. We followed the multivariate Granger causality toolbox for statistics in Granger causality analysis²⁰, with multiple comparisons corrected by the false discovery rate method (Granger *F* test). For other comparisons, two-sided or one-sided paired or unpaired *t*-tests were used.

Reporting summary

Further information on research design is available in the Nature Portfolio Reporting Summary linked to this article.

Data availability

Large raw image data from wide-field imaging and two-photon imaging are available upon request from the authors. Source data are provided with this paper.

Code availability

Links for open-source toolboxes used in this study are provided. Custom-made MATLAB codes for wide-field imaging processing, sleep scoring and mouse facial expression analysis are deposited on GitHub (https://github.com/Yoyo666222/Liulab2022_NN). Code used for additional analyses is available from the corresponding author upon reasonable request.

References

40. Han, W. et al. Integrated control of predatory hunting by the central nucleus of the amygdala. *Cell* **168**, 311–324 (2017).
41. Barger, Z., Frye, C. G., Liu, D., Dan, Y. & Bouchard, K. E. Robust, automated sleep scoring by a compact neural network with distributional shift correction. *PLoS ONE* **14**, e0224642 (2019).
42. Meng, Q. et al. Tracking eye movements during sleep in mice. *Front. Neurosci.* **15**, 616760 (2021).
43. Vollmer, M. A robust, simple and reliable measure of heart rate variability using relative RR intervals. in *Computing in Cardiology* **42**, 609–612 (2015).
44. Dana, H. et al. Sensitive red protein calcium indicators for imaging neural activity. *eLife* <https://doi.org/10.7554/eLife.12727> (2016).
45. Liu, D. et al. A common hub for sleep and motor control in the substantia nigra. *Science* **367**, 440–445 (2020).
46. Song, J. H. et al. Precise mapping of single neurons by calibrated 3D reconstruction of brain slices reveals topographic projection in mouse visual cortex. *Cell Rep.* **31**, 107682 (2020).
47. Vesuna, S. et al. Deep posteromedial cortical rhythm in dissociation. *Nature* **586**, 87–94 (2020).
48. Cardoso, J. F. High-order contrasts for independent component analysis. *Neural Comput.* **11**, 157–192 (1999).
49. Franklin, K. B. J. & Paxinos, G. Paxinos and Franklin's the Mouse Brain in Stereotaxic Coordinates, Compact: The Coronal Plates and Diagrams (Academic Press, 2008).
50. Pnevmatikakis, E. A. & Giovannucci, A. NoRMCorre: an online algorithm for piecewise rigid motion correction of calcium imaging data. *J. Neurosci. Methods* **291**, 83–94 (2017).
51. Pnevmatikakis, E. A. et al. Simultaneous denoising, deconvolution and demixing of calcium imaging data. *Neuron* **89**, 285–299 (2016).
52. Zhou, P. et al. Efficient and accurate extraction of in vivo calcium signals from microendoscopic video data. *eLife* <https://doi.org/10.7554/eLife.28728> (2018).

Acknowledgements

We thank M. M. Poo, Y. Yang and S. Xu for helpful comments; J. Tang and Y. Pan for tracing and histology; L. Kang for obtaining and breeding transgenic mice; S. Gong for mouse drawings; and X. Ge for useful information on the wide-field imaging system and discussion on the wide-field imaging data. This work was supported by the National Science and Technology Innovation 2030 grant (2022ZD0206100), the Shanghai Municipal Science and Technology Major Project (2018SHZDZX05 and 20JC1419500), a Lingang Laboratory grant (LG-QS-202203-01) and a Lingang Laboratory & National Key Laboratory of Human Factors Engineering joint grant.

Author contributions

Y.D. and D.L. designed the experiments and wrote the manuscript. Y.D. performed most of the experiments and data analysis. Y.D. developed the deep learning algorithm for online sleep scoring and established methods for facial expression analysis. J.L. performed part of the optogenetic experiments and histology. M.Z. performed part of two-photon imaging experiments, retrograde tracing and whole-brain mapping. D.L. supervised all aspects of the project.

Competing interests

The authors declare no competing interests.

Additional information

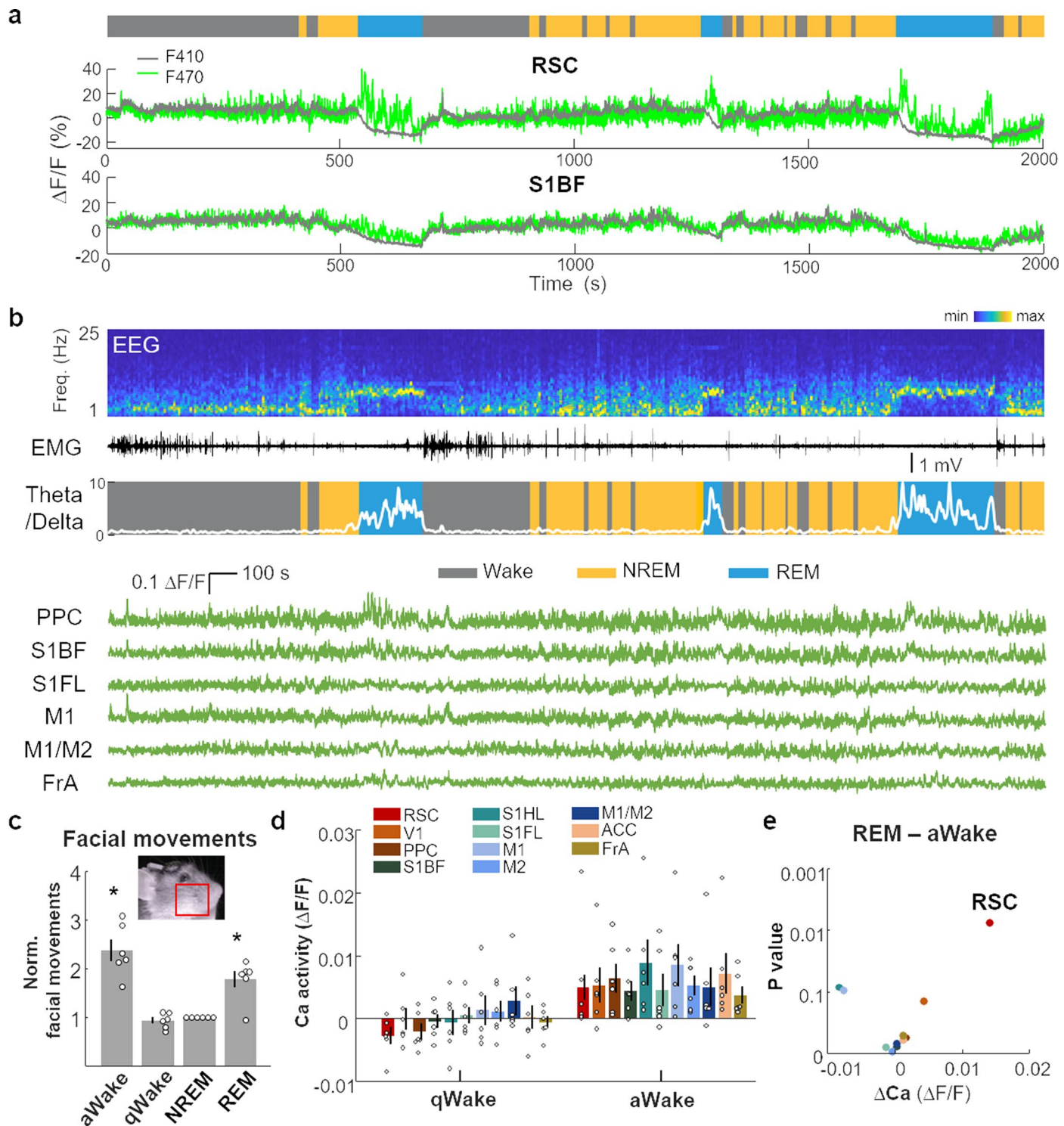
Extended data is available for this paper at <https://doi.org/10.1038/s41593-022-01195-2>.

Supplementary information The online version contains supplementary material available at <https://doi.org/10.1038/s41593-022-01195-2>.

Correspondence and requests for materials should be addressed to Danqian Liu.

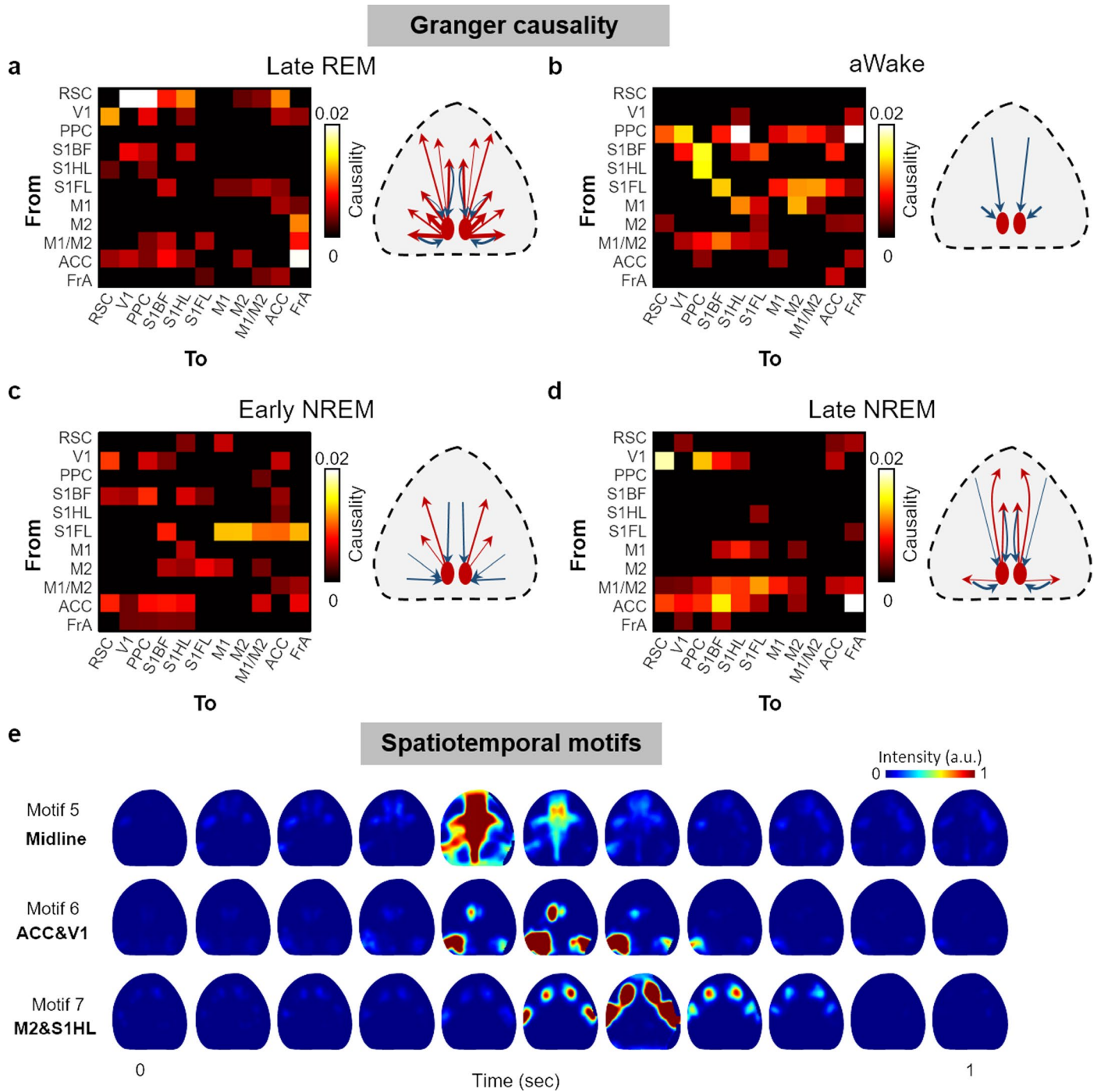
Peer review information *Nature Neuroscience* thanks Pierre-Hervé Luppi, Yueqing Peng and the other, anonymous, reviewer(s) for their contribution to the peer review of this work.

Reprints and permissions information is available at www.nature.com/reprints.



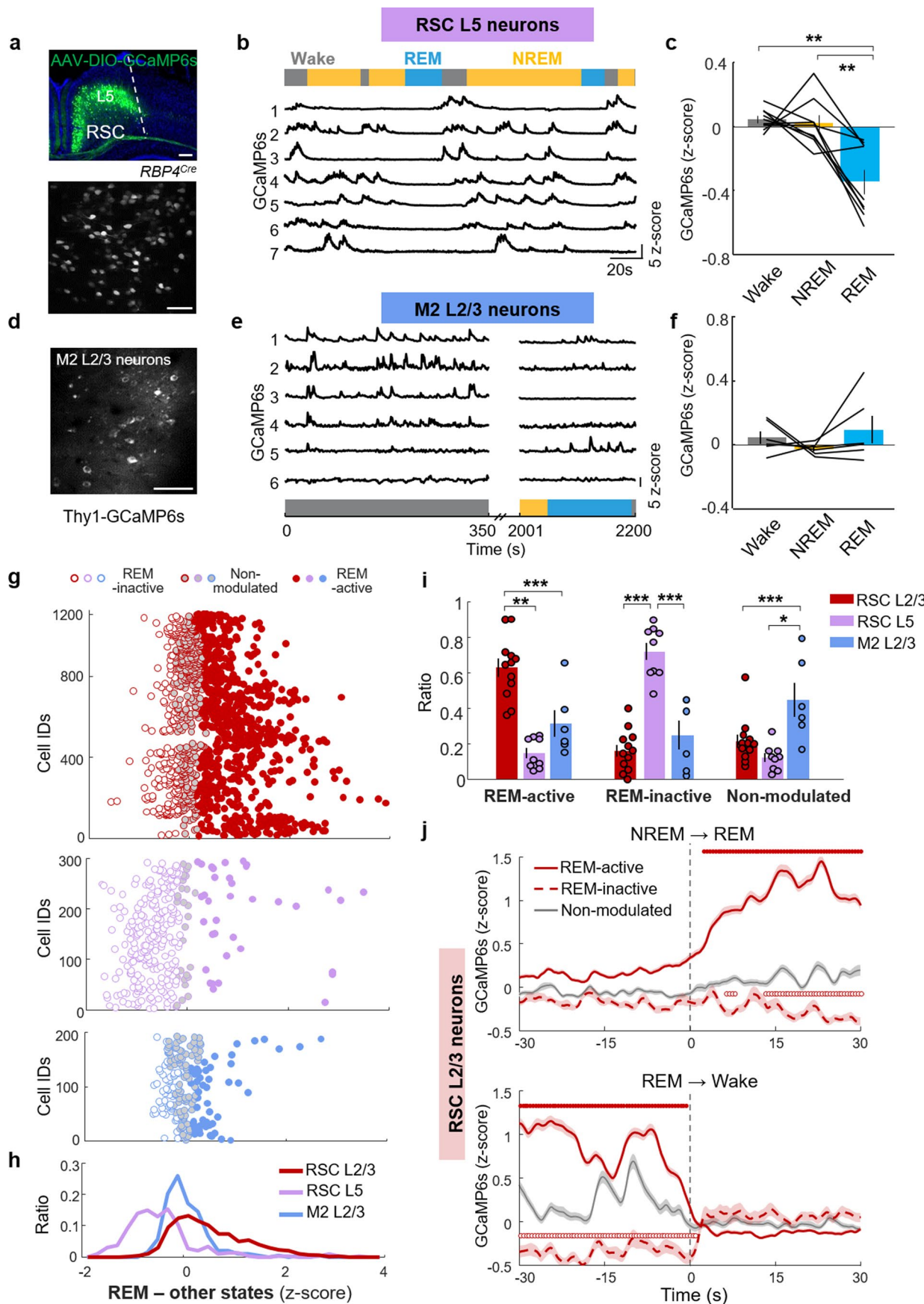
Extended Data Fig. 1 | Activity of cortical areas across brain states. **a**, Raw fluorescence signals of RSC and S1BF excited by sequential 410 nm or 470 nm light. Shown are separated $\Delta F/F$ Ca^{2+} signals for F410 and F470, together with EEG spectrogram, EMG trace and brain states. **b**, Example F410-corrected Ca^{2+} traces ($\Delta F/F$) for 6 cortical areas together with EEG spectrogram, EMG trace, EEG theta/delta ratio and color-coded brain states, during a same recording period as data shown in Fig. 1d. **c**, Total facial movements during active wake (aWake), quiet wake (qWake), NREM sleep or REM sleep ($n = 6$ sessions from 5 mice). The red box denotes facial area used for calculating facial movements. For each mouse the amplitude of facial movements was normalized by that of NREM state before averaged across mice. $P_{(\text{aWake vs NREM})} = 0.0015$; $P_{(\text{qWake vs NREM})} = 0.36$; $P_{(\text{REM vs NREM})} = 0.0063$. * $P < 0.05$, two-sided paired t test. **d**, Average Ca^{2+} activity during aWake and qWake state ($n = 6$ sessions from 5 mice). **e**, Activity difference between REM sleep and aWake state, with statistical significance (two-sided paired t test) plotted against difference in average Ca^{2+} $\Delta F/F$. Error bars, SEM.

red box denotes facial area used for calculating facial movements. For each mouse the amplitude of facial movements was normalized by that of NREM state before averaged across mice. $P_{(\text{aWake vs NREM})} = 0.0015$; $P_{(\text{qWake vs NREM})} = 0.36$; $P_{(\text{REM vs NREM})} = 0.0063$. * $P < 0.05$, two-sided paired t test. **d**, Average Ca^{2+} activity during aWake and qWake state ($n = 6$ sessions from 5 mice). **e**, Activity difference between REM sleep and aWake state, with statistical significance (two-sided paired t test) plotted against difference in average Ca^{2+} $\Delta F/F$. Error bars, SEM.



Extended Data Fig. 2 | Cortex-wide neuronal activity dynamics across brain states. **a-d**, Matrix of Granger causality between each pair of 11 cortical areas (left) and summary of causality between RSC and other areas (right), during late REM sleep (a), aWake state (b), early NREM sleep (c) and late NREM sleep (d). Data from 6 sessions from 5 mice were pooled for these analysis. Note that the uppermost row is the causality from RSC to other 10 areas. Causality with $P < 0.01$

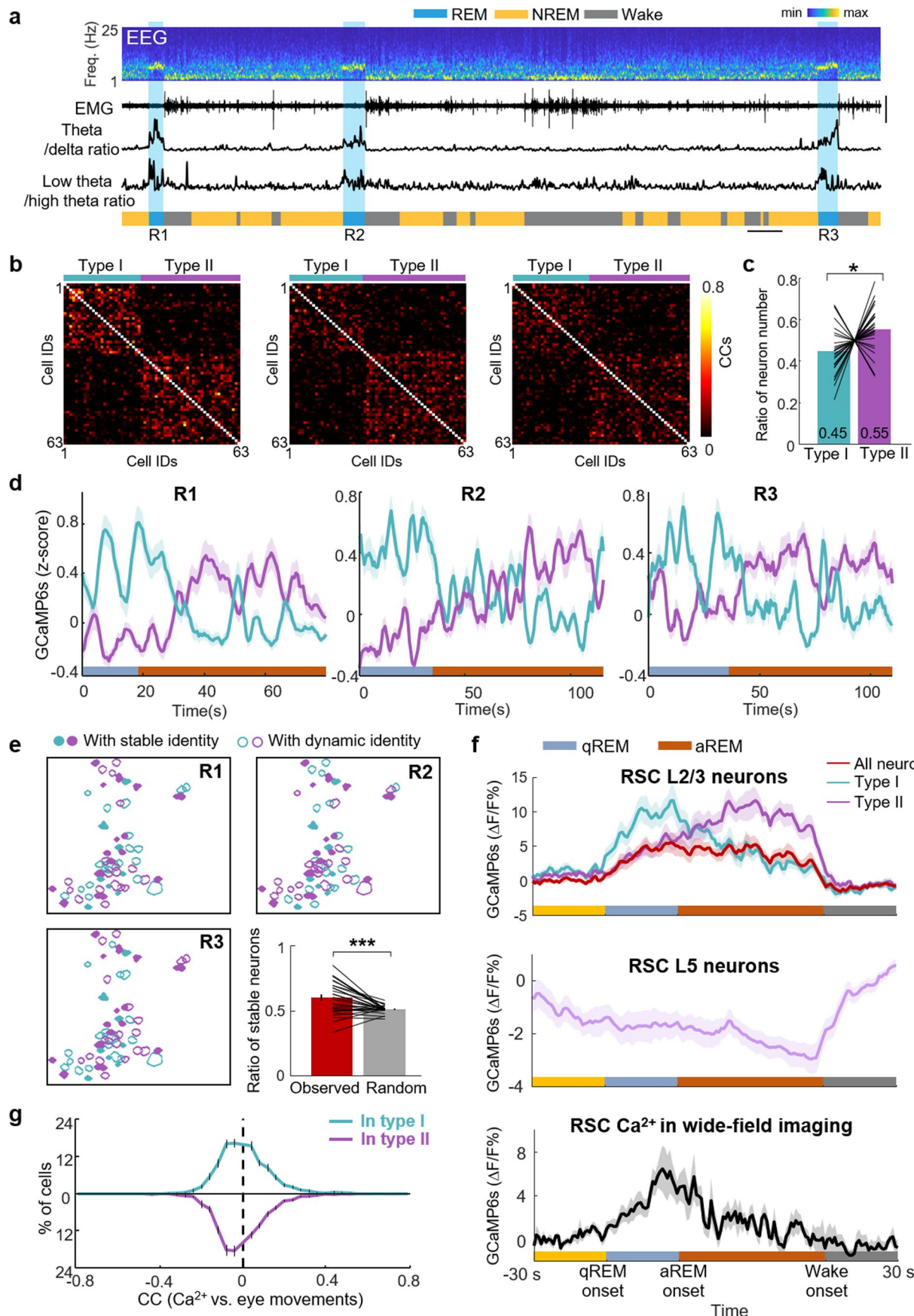
(Granger's F-test) was shown after correction for multiple comparisons by false discovery rate. Red arrows, from RSC to other modules; Blue arrows, from other modules to RSC. **e**, Common spatiotemporal motifs of cortex-wide Ca^{2+} activity. Time courses of common motifs 5 to 7 as shown in (Fig. 2c-e) showing spatiotemporal patterns of neuronal Ca^{2+} activity across dorsal cortex. The intensity scale is normalized separately for each motif.



Extended Data Fig. 3 | See next page for caption.

Extended Data Fig. 3 | Two-photon imaging of cortical neuronal activities across brain states. **a**, Top: fluorescence image of RSC in a *RBP4*^{Cre} mouse injected with AAV-DIO-GCaMP6s. Scale bar: 200 μ m. Bottom: example field of view for two-photon imaging. Scale bar: 50 μ m. **b**, Example Ca^{2+} traces of RSC L5 neurons together with color-coded brain states. **c**, Average Ca^{2+} activity of RSC L5 neurons across sleep states. Each line indicates averaged Ca^{2+} activity for all identified neurons from one recording session ($n = 9$ sessions from 4 mice). $P_{(\text{Wake vs NREM})} = 0.72$; $P_{(\text{Wake vs REM})} = 0.0023$; $P_{(\text{NREM vs REM})} = 0.0012$; ** $P < 0.005$, two-sided paired t test. **d-f**, Similar to a-c, but for L2/3 neurons in the M2 of Thy1-GCaMP6s mice. Data were from $n = 6$ sessions in 4 mice. $P > 0.1$ for all comparisons. $P_{(\text{Wake vs NREM})} = 0.22$; $P_{(\text{Wake vs REM})} = 0.85$; $P_{(\text{NREM vs REM})} = 0.10$. Scale bar in d: 50 μ m. **g-h**, Scatter (g) or line (h) plots showing the distribution of the activity difference between REM sleep and other states, for RSC L2/3 neurons ($n = 1238$ neurons from 6 mice), RSC L5 neurons ($n = 289$ from 4 mice) and M2

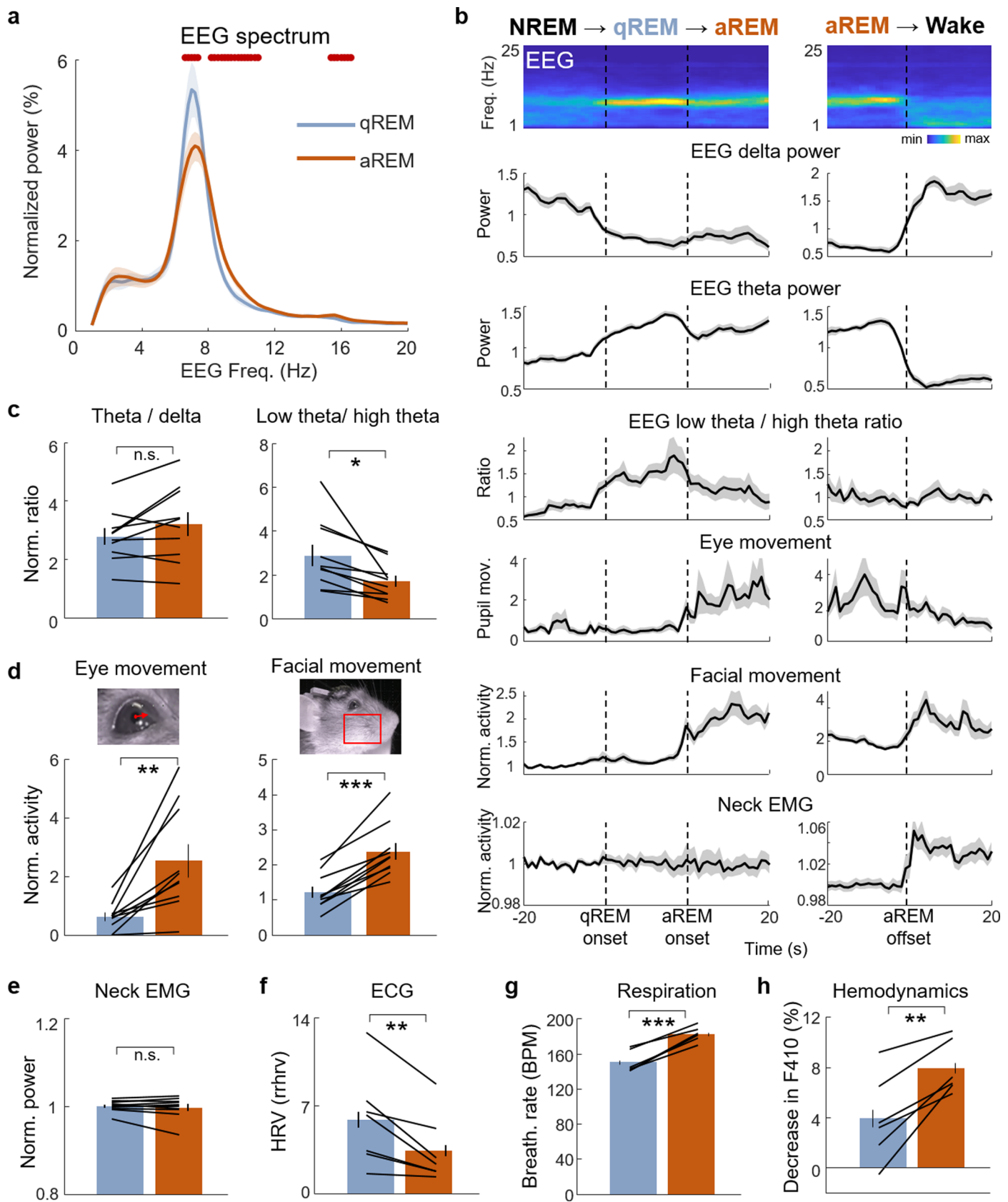
L2/3 neurons ($n = 193$ from 4 mice). **i**, Percentages of REM-active, REM-inactive and non-modulated neurons in RSC L2/3 ($n = 12$ sessions from 6 mice), RSC L5 ($n = 9$ sessions from 4 mice) or M2 L2/3 ($n = 6$ sessions from 4 mice). * $P < 0.05$, ** $P < 0.01$, *** $P < 0.001$, two-sided unpaired t test. **j**, Averaged Ca^{2+} activities for REM-active ($n = 706$ neurons), REM-inactive ($n = 188$) and non-modulated ($n = 344$) neurons in the L2/3 of RSC, at NREM \rightarrow REM (top) or REM \rightarrow wake (bottom) transitions (from 6 mice). The same dataset were used as the top panel in g. Vertical lines, transition time points. Dotted lines above the averaged traces indicate time points that are significantly different from baseline (-30 s to -6 s before NREM \rightarrow REM, or 6 s to 30 s after REM \rightarrow wake). Closed dots: $P < 0.05$ for REM-active neurons; open dots: $P < 0.05$ for REM-inactive neurons. $P > 0.1$ for non-modulated neurons. Kruskal-Wallis tests with Dunn's correction for multiple comparison. Note that the latency for significant activity increase of REM-active neurons was 2.3 s. Error bars or shadings, SEM.



Extended Data Fig. 4 | See next page for caption.

Extended Data Fig. 4 | RSC population neuronal activity encodes REM substages. **a**, Example EEG spectrogram, EMG trace, EEG theta/delta ratio, low theta/high theta ratio and color-coded brain states. Blue shadings show three REM episodes in a same recording session. **b**, Visualization of the two CC clusters of RSC neuronal activity in the same three REM episodes as shown in a. REM-active neurons ($n = 63$ in a recording session with 115 identified neurons) were used in this analysis. **c**, The ratio of cell numbers for type I and type II neuron ($n = 27$ episode from 6 mice). $*P = 0.026$, two-sided paired t test. Error bars, SEM. **d**, Averaged neuronal activities of type I and type II neurons in the three REM episodes, together with color-coded two REM substages. Shadings, SEM. **e**, Maps of recorded RSC cells in the three REM episodes as shown in a,b,d. Cells defined as type I were color-coded in cyan, and cells defined as type II were in purple. Note that neurons with stable identity across REM episodes were color-filled.

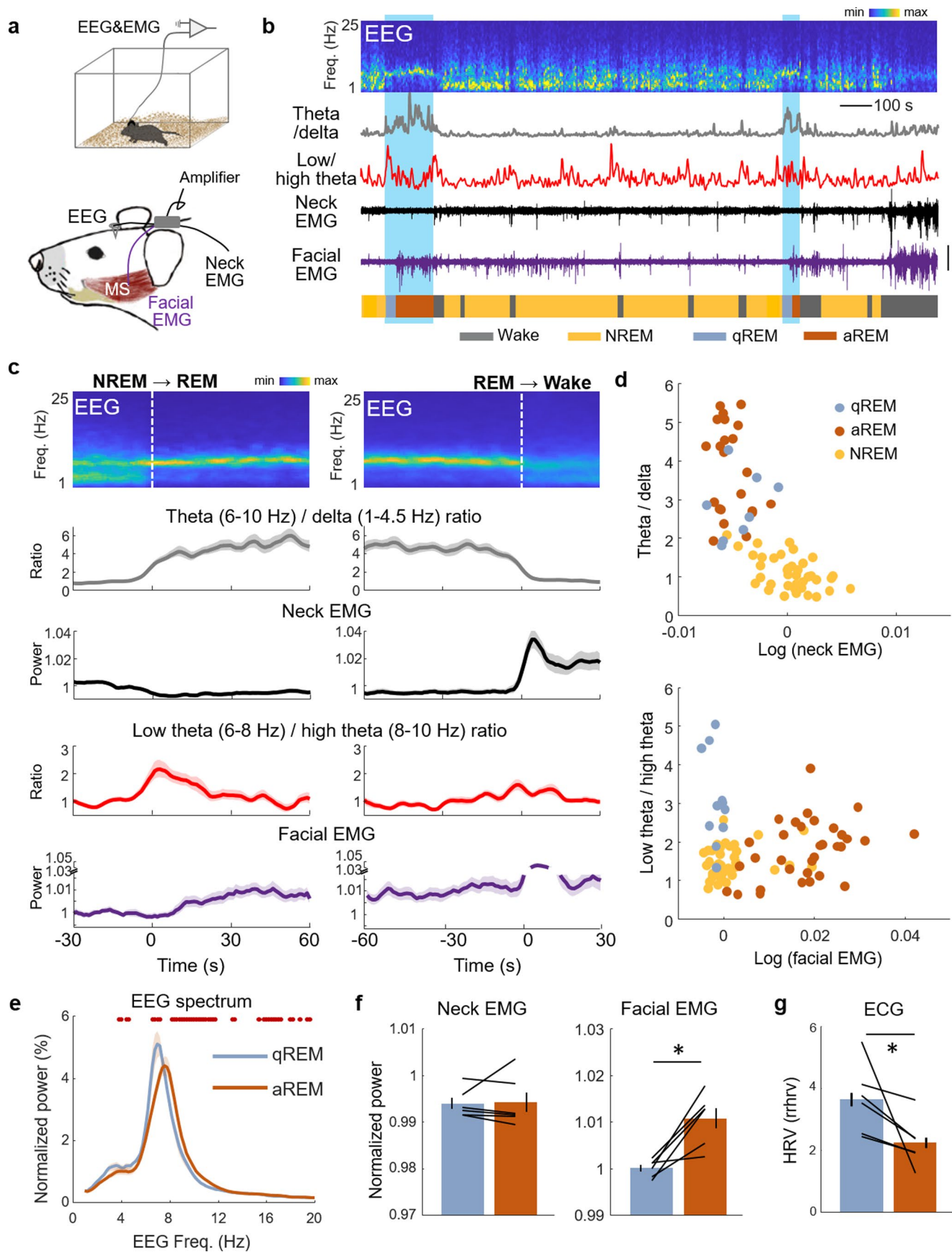
Bottom right, comparison of the percentage of neurons with stable identity in observed data to that estimated from random sampling, for each pair of REM episodes ($n = 28$ pairs from 6 mice). $***P = 0.0004$, two-sided paired t test. Error bars, SEM. **f**, Averaged Ca^{2+} activity of RSC L2/3 (top, $n = 6$ mice), RSC L5 neuron (middle, $n = 4$ mice) from two-photon imaging and total RSC activity from wide-field imaging (bottom, $n = 5$ mice) at brain state transitions. Each qREM substage was temporally compressed to one unit length, and aREM substage compressed to three unit length, before averaged over multiple episodes. Shadings, SEM. **g**, Distribution of correlation coefficient (CC: Ca^{2+} activity vs. binary labelling of eye movements) in type I&II RSC populations. The distribution was calculated for each episode before averaging across 27 REM episodes. Each line represents CC distribution for one episode. $P > 0.7$ for comparison of each CC distribution with zero ($P_{\text{TypeI}} = 0.88$, $P_{\text{TypeII}} = 0.77$), two-tail z test. Error bars, SEM.



Extended Data Fig. 5 | See next page for caption.

Extended Data Fig. 5 | Comparison of EEG power spectra and autonomic activity between the two REM substages. **a**, Normalized EEG power spectra in qREM and aREM, averaged across 10 sessions from 7 mice. Red dots indicate frequency bins that are significantly different between the two substages (at $P < 0.05$, two-sided paired t test with Bonferroni multiple comparison correction). Note that qREM has a significant higher power from 6.5 to 7.5 Hz, while aREM has significant higher power from 8.2 to 11 Hz. **b**, Averaged EEG spectrogram, EEG delta, theta power, low theta (6–8 Hz) to high theta (8–10 Hz) ratio, eye movements, facial movements and neck EMG power at brain state transitions. Each qREM substage was temporally compressed to one unit length. For each trace, data were normalized by that of NREM sleep before averaging across mice. Vertical lines represent transition points. Shadings, SEM. **c**, EEG theta/delta ratio (left) and low theta/high theta ratio (right) in qREM and aREM substages ($n = 10$ sessions from 7 mice). $P_{(\text{theta/delta})} = 0.13$; $P_{(\text{Low/high theta})} = 0.04$. **d**,

Normalized eye movements (measured by pupil movements, left), and facial movements (right) in qREM and aREM substages ($n = 10$ sessions from 7 mice). The red box denotes facial area used for calculating facial movements. $P_{(\text{Eye movement})} = 0.0033$; $P_{(\text{Facial movement})} = 0.000024$. **e**, Normalized neck EMG power in qREM and aREM substages ($n = 10$ sessions from 7 mice). $P = 0.42$. **f**, Heart rate variability (HRV), measured by relative RR intervals, in qREM and aREM substages ($n = 7$ sessions from 5 mice). Note that lower HRV indicates higher sympathetic activation. $P = 0.0083$. **g**, Respiration rate in qREM and aREM substages ($n = 6$ sessions from 3 mice). $P = 0.00025$. **h**, Cortical hemodynamics in qREM and aREM substages, reflected by decrease of fluorescence signal excited by 410 nm light ($n = 6$ sessions from 5 mice). For each session, the decrease in F410 was normalized by that of NREM sleep before averaged across mice ($P = 0.0044$). * $P < 0.05$, ** $P < 0.01$, *** $P < 0.001$, two-sided paired t test. Error bars and shadings, SEM.



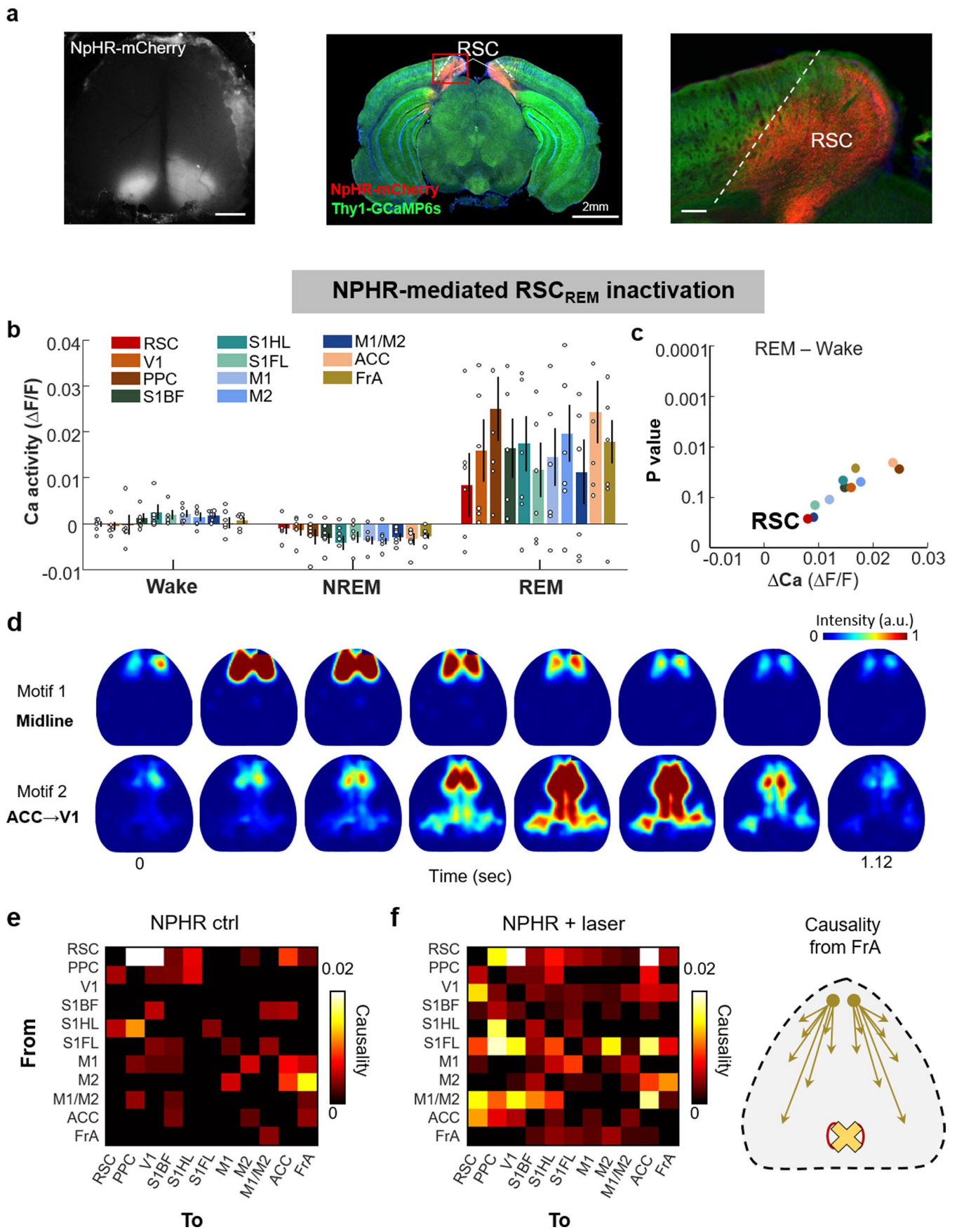
Extended Data Fig. 6 | See next page for caption.

Extended Data Fig. 6 | Facial EMG recording revealed two REM substages in freely-moving mice. **a**, Schematics for EEG, neck EMG and facial EMG recording in a freely-moving mouse. MS, masseter muscle. **b**, Example EEG spectrogram, EEG theta (6–10 Hz) to delta (1–4.5 Hz) ratio, low theta (6–8 Hz) to high theta (8–10 Hz) ratio, neck EMG, facial EMG trace and color-coded four brain states. **c**, Averaged EEG spectrogram, EEG theta/delta ratio, low theta/high theta ratio, neck EMG, and facial EMG power at NREM → REM sleep, and REM sleep→Wake transitions, averaged across 6 recording sessions from 4 mice. For each trace, data were normalized by that of NREM sleep before averaging across sessions. **d**, Top: example scatter plot for theta/delta ratio and neck EMG power. Bottom: example scatter plot for low theta/high theta ratio and facial EMG power. Each dot represents data in a 5-s bin in the example recording session in (b). Data from

NREM sleep in 100 s preceding the two REM episodes were also shown.

e, Normalized EEG power spectra during qREM and aREM, averaged from 4 mice. Red dots indicate frequency bins that are significantly different between the two substages, at $P < 0.05$ (two-sided paired t test with Bonferroni multiple comparison correction). **f**, Normalized neck EMG (left) or facial EMG (right) in qREM and aREM. The EMG amplitude was normalized by that of NREM sleep before averaged across recording sessions ($n = 6$ sessions from 4 mice). Each line represents one recording session. $P_{(\text{Neck EMG})} = 0.85$; $P_{(\text{Facial EMG})} = 0.0064$.

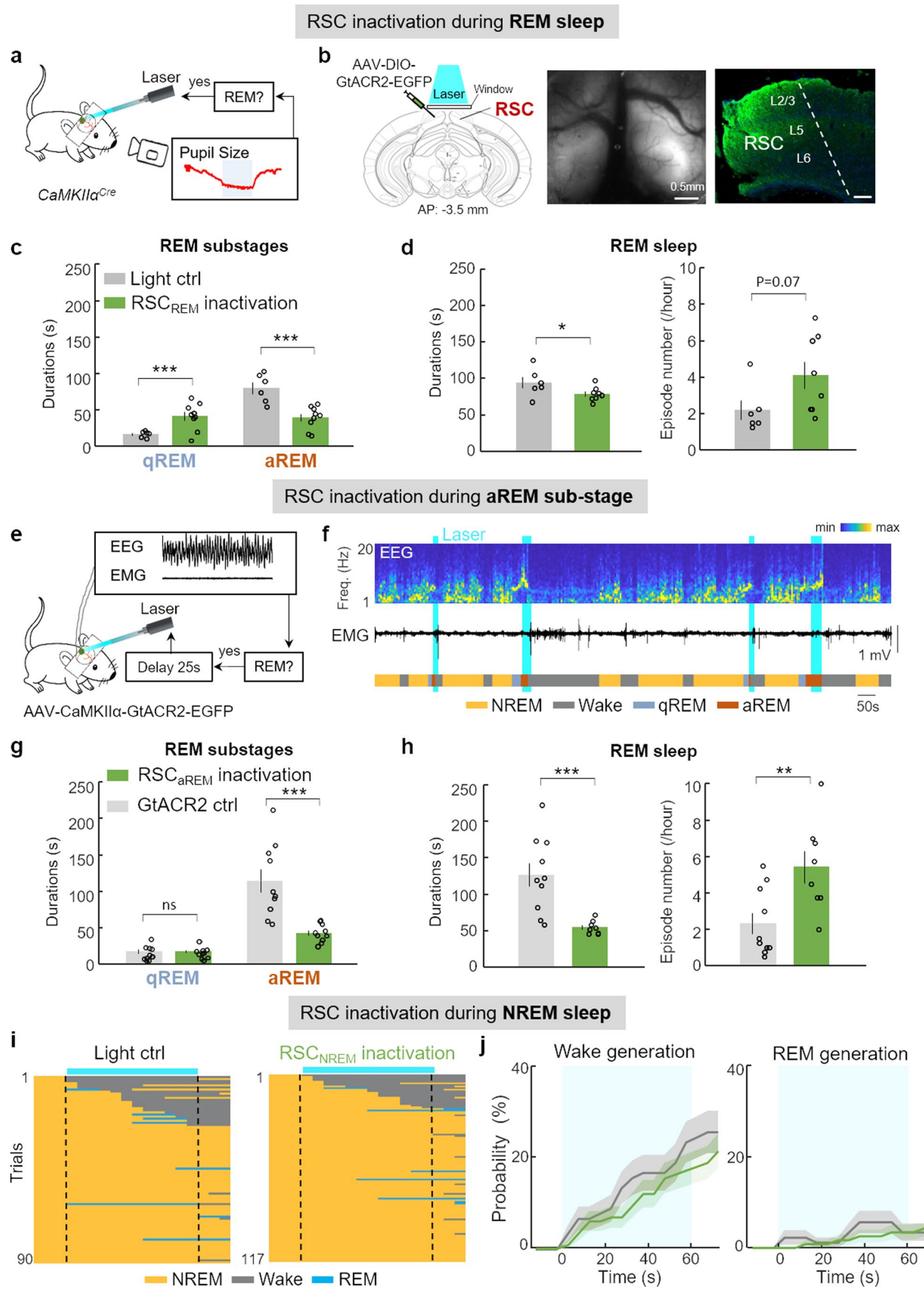
g, Heart rate variability (HRV), measured by relative RR intervals, in qREM and aREM substages ($n = 6$ sessions from 4 mice, $P = 0.033$). Each line represents one recording session. * $P < 0.05$, two-sided paired t test. Error bars or shadings, SEM.



Extended Data Fig. 7 | See next page for caption.

Extended Data Fig. 7 | Optogenetic inactivation altered cortical neuronal dynamics. **a**, Images showing expression of AAV-CaMKII α -NpHR3.0-mCherry in the RSC of Thy1-GCaMP6s mouse. Left: top view of wide-field imaging through a cortex-wide transparent window, excited by 593 nm light. Scale bar: 500 μ m. Middle: a fluorescence image of a coronal brain slice showing mCherry expression. Scale bar: 2 mm. Right: image with higher magnification of the region in red box. Scale bar: 200 μ m. **b**, Average Ca^{2+} activity across brain states in RSC_{REM} inactivation mice (6 sessions from 4 mice). **c**, Activity difference between REM sleep and wake state, with statistical significance (two-sided paired *t* test) plotted against difference in average Ca^{2+} $\Delta F/F$. Error bars, SEM. **d**, Time courses of 2 new

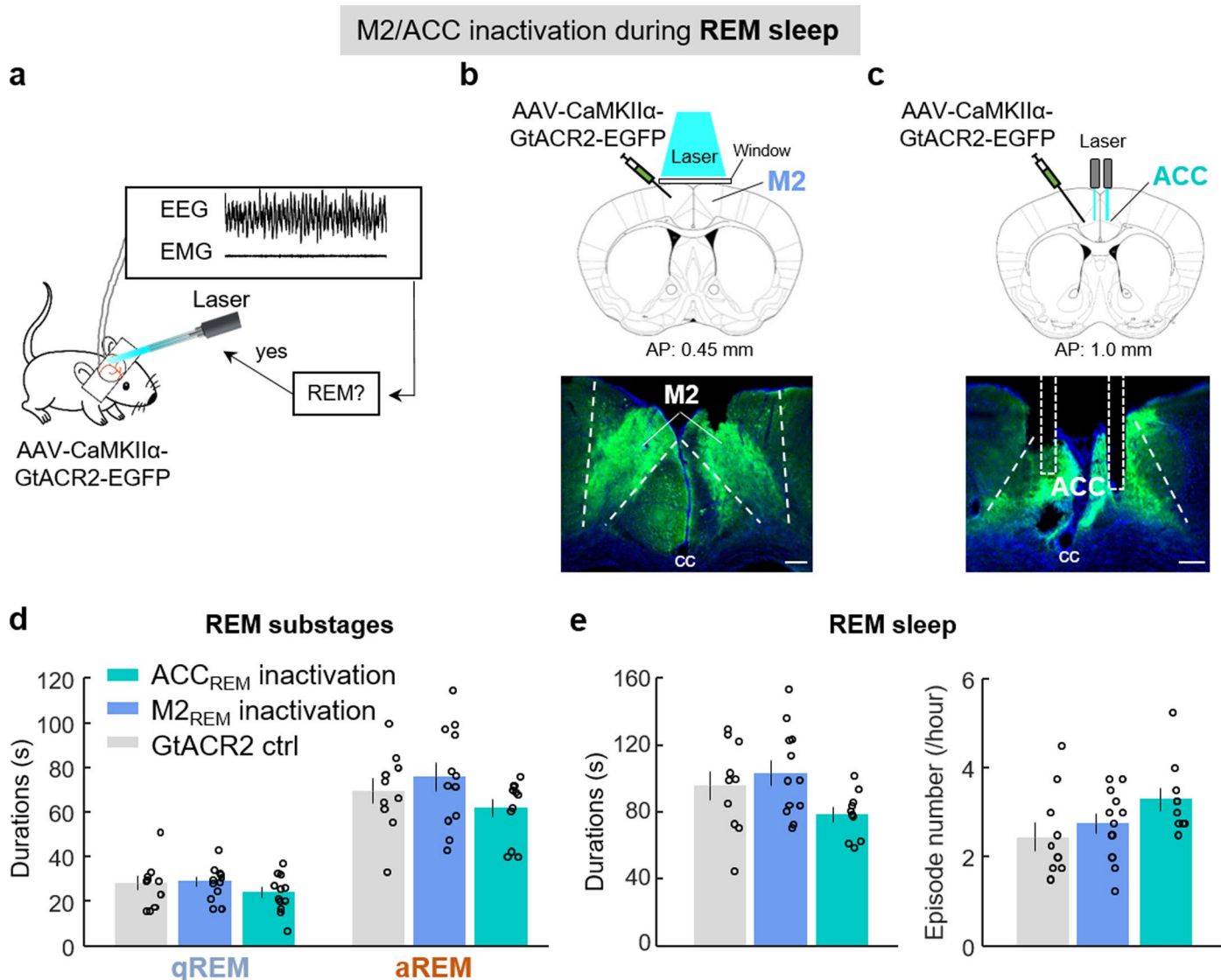
motifs in RSC_{REM} inactivation mice showing spatiotemporal patterns of neuronal Ca^{2+} activity across dorsal cortex. The intensity scale is normalized separately for each motif. **e**, Matrix of Granger causality between each pair of 11 cortical areas during REM sleep, in NPHR-expressing mice without light stimulation. Noted that the uppermost row is causality from RSC to other 10 modules. Causality with $P < 0.01$ (Granger's *F*-test) was shown after correction for multiple comparisons by false discovery rate. **f**, Left, same as (e), but for Granger causality in mice with NPHR-mediated RSC_{REM} inactivation. Right, Summary of causality from FrA in RSC_{REM} inactivation mice.



Extended Data Fig. 8 | See next page for caption.

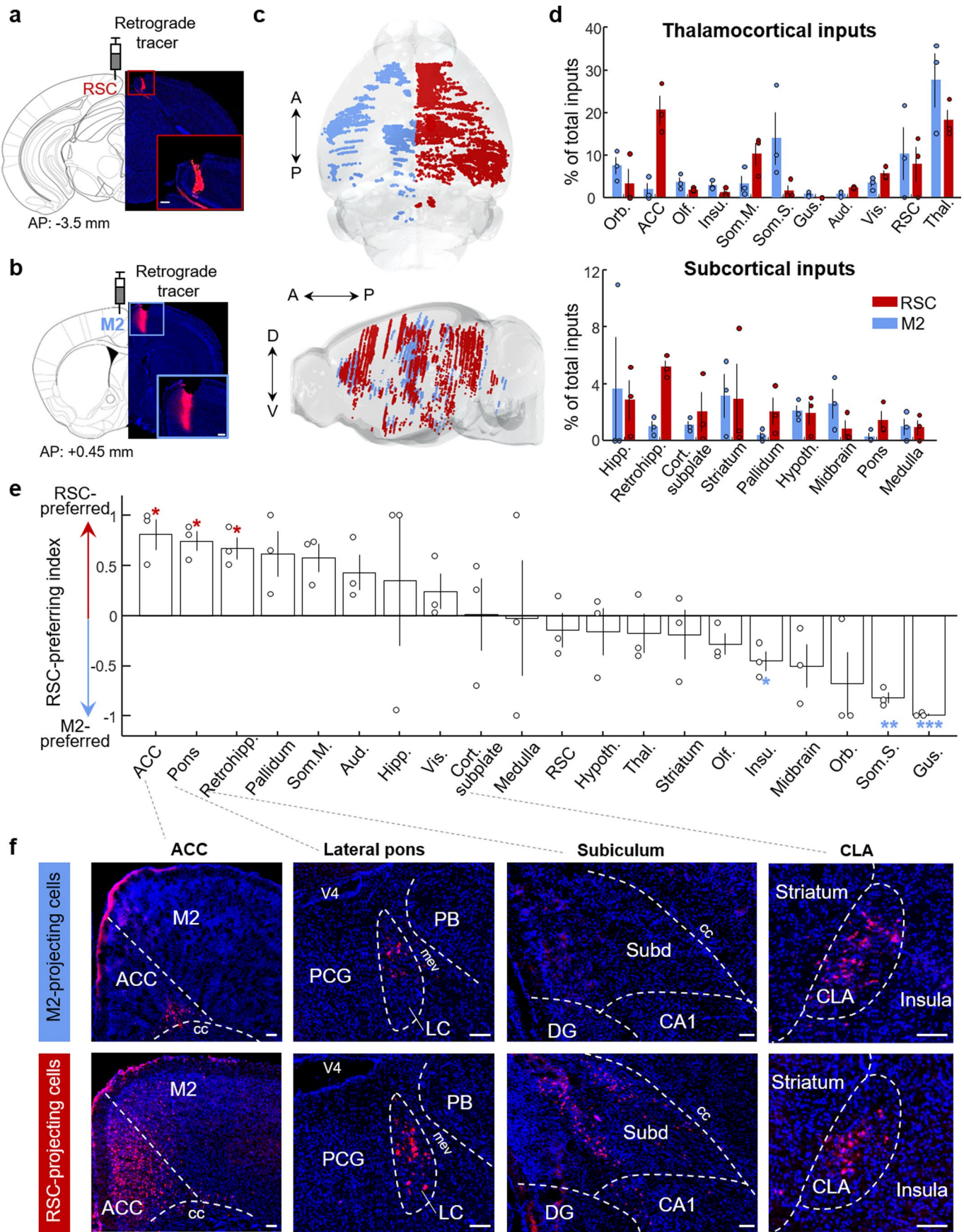
Extended Data Fig. 8 | Effects of optogenetic inactivation of RSC during REM sleep, aREM substage, or NREM sleep. **a**, Schematic for close-loop optogenetic inactivation during REM sleep based on pupil size change. **b**, Left: schematic for optogenetic inactivation through a transparent window covering RSC bilaterally. Right: top view wide-field image and fluorescence image showing GtACR2-EGFP expression in RSC. Scale bar: 200 μ m. **c-d**, Duration of REM substages (c), and episode duration or episode number of total REM sleep (d) in light control (6 sessions from 4 mice) and RSC_{REM} inactivation group (8 sessions from 3 mice). Each dot represents averaged data from one recording session. $P_{(qREM\ duration)}=0.00047$; $P_{(aREM\ duration)}=0.00071$; $P_{(REM\ duration)}=0.027$; $P_{(REM\ episode)}=0.07$. * $P < 0.05$, *** $P < 0.001$, two-sided unpaired t test. **e**, Schematic for close-loop optogenetic inactivation during aREM substage. **f**, EEG spectrogram, EMG trace and color-

coded brain states from an example RSC_{aREM} inactivation recording session. Blue shadings show laser period. **g-h**, similar to c-d, but for RSC_{aREM} inactivation. GtACR2 control: 10 sessions from 4 mice, RSC_{aREM} inactivation: 8 sessions from 3 mice. $P_{(qREM\ duration)}=0.98$; $P_{(aREM\ duration)}=0.00042$; $P_{(REM\ duration)}=0.00053$; $P_{(REM\ episode\ number)}=0.0037$. ** $P < 0.01$, *** $P < 0.001$, two-sided unpaired t test. **i**, Color-coded brain states for all NREM trials (with the onset of 1-min blue laser fell in NREM sleep) in light control (14 sessions from 7 mice) and RSC_{NREM} inactivation group (14 sessions from 5 mice). Vertical lines represent the laser onset and offset. **j**, Cumulative probability for wake generation or REM sleep generation during 60-s laser stimulation. $P > 0.8$, bootstrap, 10000 iteration. Blue shading represents laser period. Error bars and shadings, SEM.



Extended Data Fig. 9 | Optogenetic inactivation of M2 or ACC during REM sleep. **a**, Schematic for REM sleep-specific optogenetic inactivation. **b**, Top: schematic for optogenetic inactivation through a transparent window covering M2 bilaterally. Bottom: fluorescence image showing GtACR2-EGFP expression in M2. **c**, Top, schematic for optogenetic inactivation through optic fibers; Bottom, fluorescence image showing GtACR2-EGFP expression. Scale bars: 200 μ m. **d-e**,

Duration of REM substages (d), and episode duration or episode number of total REM sleep (e) in GtACR2 control (10 sessions from 6 mice), ACC_{REM} inactivation (10 sessions from 3 mice), and M2_{REM} inactivation group (12 sessions from 5 mice). Each dot represents averaged data from one recording session. $P > 0.05$ for all comparisons between the inactivation and control groups, two-sided unpaired t test. Error bars, SEM.



Extended Data Fig. 10 | See next page for caption.

Extended Data Fig. 10 | Whole-brain mapping of inputs to the RSC and M2 **a**, **Schematic for injection of retrograde tracer in RSC, and fluorescence image showing the injection site.** Inset shows higher magnification of the region in red box. Scale bar: 200 μ m. **b**, Similar to a, but for M2. **c**, Example of whole-brain reconstruction of retrograde-labelled cells (also referred to as ‘inputs’) from RSC (red) or M2 (blue). Injection site is excluded. **d**, Percentages of labelled cells (referred to as ‘inputs’) in the thalamocortical areas (top) and subcortical areas (bottom), normalized by the total number of labelled cells for each mouse. Each dot represents data from one mouse (RSC: n = 3; M2: n = 3). Orb., orbital area; Olf., olfaction areas; Insu., insula area; Som.M. somatomotor areas; Som. S., somatosensory areas; Gus., gustatory areas; Aud., auditory areas; Vis., visual

areas; Thal., thalamus; Hipp., hippocampal region; Retrohipp., retrohippocampal region; Cort. Subplate, cortical subplate; Hypoth., hypothalamus. Error bars, SEM. **e**, Summary showing the preference for each region projecting to the RSC. In each pair of tracing experiments (n = 3 pairs), the RSC-preferring index for each region was calculated as (input to RSC-input to M2) / (input to RSC + input to M2). * $P_{ACC} = 0.034$, $P_{Pons} = 0.017$, $P_{Retrohipp.} = 0.025$, $P_{Insu} = 0.045$, ** $P_{Som.S.} = 0.0043$, *** $P_{Gus} = 0.00015$, two-sided paired t test. Error bars, SEM. **f**, Fluorescence images showing retrograde-labelled neurons projecting to M2 (top) or RSC (bottom). Cc: corpus callosum; PCG: pontine central gray; V4: fourth ventricle; mev: midbrain trigeminal nucleus; PB: parabrachial nucleus; Subd: dorsal part of the subiculum; CLA: claustrum. Scale bar: 100 μ m.

Reporting Summary

Nature Portfolio wishes to improve the reproducibility of the work that we publish. This form provides structure for consistency and transparency in reporting. For further information on Nature Portfolio policies, see our [Editorial Policies](#) and the [Editorial Policy Checklist](#).

Statistics

For all statistical analyses, confirm that the following items are present in the figure legend, table legend, main text, or Methods section.

n/a Confirmed

- The exact sample size (n) for each experimental group/condition, given as a discrete number and unit of measurement
- A statement on whether measurements were taken from distinct samples or whether the same sample was measured repeatedly
- The statistical test(s) used AND whether they are one- or two-sided
 - Only common tests should be described solely by name; describe more complex techniques in the Methods section.*
- A description of all covariates tested
- A description of any assumptions or corrections, such as tests of normality and adjustment for multiple comparisons
- A full description of the statistical parameters including central tendency (e.g. means) or other basic estimates (e.g. regression coefficient) AND variation (e.g. standard deviation) or associated estimates of uncertainty (e.g. confidence intervals)
- For null hypothesis testing, the test statistic (e.g. F , t , r) with confidence intervals, effect sizes, degrees of freedom and P value noted
 - Give P values as exact values whenever suitable.*
- For Bayesian analysis, information on the choice of priors and Markov chain Monte Carlo settings
- For hierarchical and complex designs, identification of the appropriate level for tests and full reporting of outcomes
- Estimates of effect sizes (e.g. Cohen's d , Pearson's r), indicating how they were calculated

Our web collection on [statistics for biologists](#) contains articles on many of the points above.

Software and code

Policy information about [availability of computer code](#)

Data collection

All commercial software to collect the data in this study are described, including Micromanager 2.0gamma for wide-field imaging, Scanimate 3.8.1 for two-photon imaging, Bonsai 2.6.3 for video recording and photometry recording, and open ephys v0.4.6-windows, TDT Drivers/ RPvdsEx v85 (TDT RZ5 amplifier) or Hypnos (Bio-signal sleep recording system) for sleep recording.

Data analysis

We used MATLAB(2019b) for data analysis. Open source toolboxes were used for data analysis: HRVTool version 1.04 for ECG analysis, JADER for ICA analysis, multivariate Granger causality toolbox v1.2 for Granger causality analysis, seqNMF for motif analysis, NoRMCorre for motion corection of two photon images, CNMF-E for extraction of single neuron, AMaSiNe 1.1.1 for whole-brain mapping. The links of open-source toolboxes were provided in the Method. Custom codes for wide-field imaging analysis, mouse facial expression analysis and sleep scoring were uploaded on GitHub with link provided in the Code Availability statement. Custom codes for additional analysis is available from the corresponding authors upon reasonable request.

For manuscripts utilizing custom algorithms or software that are central to the research but not yet described in published literature, software must be made available to editors and reviewers. We strongly encourage code deposition in a community repository (e.g. GitHub). See the Nature Portfolio [guidelines for submitting code & software](#) for further information.

Data

Policy information about [availability of data](#)

All manuscripts must include a [data availability statement](#). This statement should provide the following information, where applicable:

- Accession codes, unique identifiers, or web links for publicly available datasets
- A description of any restrictions on data availability
- For clinical datasets or third party data, please ensure that the statement adheres to our [policy](#)

Allen Mouse Brain Atlas (© 2015 Allen Institute for Brain Science).

Allen Brain Atlas (API. Available from: brain-map.org/api/index.html) was used as templates for 3D whole brain mapping. Source data for Figures are provided with this paper. Large image raw data from wide-field imaging and two photon imaging are available upon request from the authors.

Field-specific reporting

Please select the one below that is the best fit for your research. If you are not sure, read the appropriate sections before making your selection.

Life sciences Behavioural & social sciences Ecological, evolutionary & environmental sciences

For a reference copy of the document with all sections, see nature.com/documents/nr-reporting-summary-flat.pdf

Life sciences study design

All studies must disclose on these points even when the disclosure is negative.

Sample size	No statistical methods were used to pre-determine sample sizes but our sample sizes are similar to those reported in previous publications.
Data exclusions	No data were excluded from the analyses.
Replication	Multiple mice from independent cohorts were used. The numbers of animals, recording sessions, or neurons were clearly indicated on the graphs or in figure legends. Example plots were representative for the average result from. Histology images shown in Figures were repeated in at least three mice.
Randomization	Selection of animals for experiments was randomized. For optogenetic experiments, the sequence of with-light or without-light sessions were randomized. For comparison of sleep under head-fixed or freely moving conditions, mice were randomly assigned to groups with head-fixed sleep recording on the first day and freely-moving sleep recording on the second day, or vice versa.
Blinding	Data collection and analysis were not performed blind to the conditions of the experiments. Batch and automatic analyses were performed for control and experimental groups, yielding no subjective bias.

Reporting for specific materials, systems and methods

We require information from authors about some types of materials, experimental systems and methods used in many studies. Here, indicate whether each material, system or method listed is relevant to your study. If you are not sure if a list item applies to your research, read the appropriate section before selecting a response.

Materials & experimental systems

n/a	Involved in the study
<input checked="" type="checkbox"/>	Antibodies
<input checked="" type="checkbox"/>	Eukaryotic cell lines
<input checked="" type="checkbox"/>	Palaeontology and archaeology
<input type="checkbox"/>	Animals and other organisms
<input checked="" type="checkbox"/>	Human research participants
<input checked="" type="checkbox"/>	Clinical data
<input checked="" type="checkbox"/>	Dual use research of concern

Methods

n/a	Involved in the study
<input checked="" type="checkbox"/>	ChIP-seq
<input checked="" type="checkbox"/>	Flow cytometry
<input checked="" type="checkbox"/>	MRI-based neuroimaging

Animals and other organisms

Policy information about [studies involving animals](#); [ARRIVE guidelines](#) recommended for reporting animal research

Laboratory animals

Thy1-GCaMP6s (GP4.3Dkim, Jackson Laboratory stock, 024275) mice, CaMKIIαCre (005359), RBP4Cre (MMRRC 031125) and C57BL/6 mice, 2-6 month-old male and female mice were used for all experiments.

Wild animals

The study does not involve wild animals.

Field-collected samples

The study does not involve samples collected from the field.

Ethics oversight

All procedures were approved by the Animal Care and Use Committees of the Center for Excellence in Brain Science and Intelligence Technology, Chinese Academy of Sciences.

Note that full information on the approval of the study protocol must also be provided in the manuscript.